2023-07-25

Comparison of Compact Very High Frequency (VHF) Antennas for Small Airborne Ground Penetrating Radar

Tayler Austen Livingston
Brigham Young University

Comparison of Compact Very High Frequency (VHF) Antennas for Small Airborne Ground Penetrating Radar

Tayler Austen Livingston

A thesis submitted to the faculty of
Brigham Young University
in partial fulfillment of the requirements for the degree of

Master of Science

David G. Long, Chair
Karl F. Warnick
Cammy K. Peterson

Department of Electrical and Computer Engineering

Brigham Young University

Comparison of Compact Very High Frequency (VHF) Antennas for Small Airborne Ground Penetrating Radar

Tayler Austen Livingston
Department of Electrical and Computer Engineering
Master of Science

BYU Engineering

Abstract

Ground penetrating radar (GPR) systems generally operate in the VHF or UHF bands because more penetration can be achieved at low frequencies. Consequently, large antennas are required, which limits their use for small airborne applications. This thesis explores various GPR antenna designs for a bi-static system that are at least operational from 225 MHz to 255 MHz and suitable for small airborne applications. The 3D electromagnetic simulation software Ansys high-frequency structure simulator (HFSS) was used to simulate various sizes of strip dipole, triangular bowtie, half elliptical bowtie, and elliptical bowtie antennas. Several physical models were constructed to validate the return loss simulation results. Additionally, simulation data is included for a wire dipole and a helical antenna. The helical antenna proved to be too large for small airborne application, so focus was placed on the dipole and bowtie designs.

The performance of the dipole and bowtie antenna models are compared by size, weight, return loss (S_{11}), peak gain, and the transmit-to-receive isolation. Out of the fourteen simulated models, twelve meet the bandwidth requirement with an average weight of 0.23 lbs. It is found that the strip dipole exhibited wider bandwidth characteristics than the triangular, elliptical, and half elliptical bowtie models, while maintaining similar weight and size. The smallest strip dipole model is 50 mm x 528 mm x 1 mm, weighs 0.17 lbs, and is operational from 225 MHz to 283 MHz. Two strip dipole test antennas were fabricated and tested. Test results confirm the simulation predictions.

Keywords: triangular bowtie antenna, half elliptical bowtie antenna, elliptical bowtie antenna, strip dipole antenna, helical antenna, VHF, compact, ground penetrating radar (GPR)

Acknowledgments

First and foremost, I am grateful for my wife Madi and her patience with me as I finished my graduate degree. I am grateful for my parents and the sacrifices they made to get me to where I am today. I am grateful for my siblings, particularly my brother Braden who encouraged me to pursue a degree in computer/electrical engineering.

I am grateful for the mentorship I received from Dr. Hung (Jacques) Loui and the opportunity he gave me to learn from and work with some of the most brilliant minds in the nation. His encouragement helped me to develop a greater passion for electromagnetics.

I also want to thank my fellow students who played key roles in my success as a graduate student: James Smith, Nate Porter, Adam Whipple, and Josh Kjar. Additionally, I want to thank Trevor Wiseman for his efforts and his willingness to further this research.

Lastly, I want to give a special thanks to Dr. David Long for seeing my potential as an undergraduate student and giving me a chance to learn and grow as one of his research assistants. His willingness to have long discussions that were tailored to my specific educational needs, were essential in my progression as a student.

Table of Contents

List of Figures

List of Tables

1 Introduction

1.1 Introduction

Radar systems operate by transmitting electromagnetic waves into the surrounding environment then receiving the portion of the waves that are reflected back toward the radar. By analyzing the timing, amplitude and the phase of the captured signal, various characteristics including the range, size, velocity, and or material type can be determined.

Ground penetrating radar (GPR) is a type of radar that is specifically used to obtain information about subsurface features. It does this by fixing the geometry between the transmitter and receiver, which are moved over the surface to detect the backscatter from materials or objects below the surface of the earth. GPR systems generally operate in the Very High Frequency (VHF) or Ultra-High Frequency (UHF) bands because better penetration can be achieved at lower frequencies. As a consequence, large antennas are required because their size is related to the wavelength of the frequency of operation.

Professors from the Geology department at Brigham Young University are interested in using ground penetrating radar to monitor the health of various glaciers in Switzerland. Unfortunately, the glaciers they wish to survey are not safely accessible by foot. Instead, they will fly a bi-static GPR on a drone over the glacier, which requires the weight for the radar, antennas, and materials used for mounting the system to the drone to be less than 5 lbs. As a result, the radar system and antennas must be lightweight and relatively compact.

For the radar electronics, we use a Lime-SDR Mini software defined radio (SDR) and a Raspberry Pi computer configured as a ground penetrating radar because it is light weight, inexpensive, and fairly versatile. The Lime-SDR Mini has been shown to be successfully implemented as a bi-static linear frequency-modulated continuous-wave radar in [1]. The radar will be operational from 225 MHz to 255 MHz, as limited by the 30 MHz maximum instantaneous bandwidth of the SDR.

1.2 Thesis Statement and Results Summary

The goal of this research is to create and compare various antenna designs that are lightweight, relatively compact, and operational from at least 225 MHz to 255 MHz. In future implementations, higher bandwidth is desired. As a result, this research looks into various antenna designs that could be

made to be operational from 225 MHz to 270 MHz. The antennas needed to be designed such that they could easily be tuned to other frequencies. The antennas considered in this study are variations of the strip dipole, triangular bowtie, half elliptical bowtie, and elliptical bowtie. Additionally, the design of a half wavelength wire dipole antenna is included for comparison data, a monofilar wire helical antenna is included upon request from an advisor, and an acorn-shaped bowtie antenna is included for personal curiosity. Each of these models were simulated and optimized with Ansys high-frequency structure simulator (HFSS) and a few designs were selected to be built and tested to validate the simulation results.

The simulations demonstrate that each model, with the exception of the two smallest triangular bowtie antennas, is capable of being operational from at least 225 MHz to 255 MHz, while maintaining a relatively compact structure. The wire dipole performs the best based on the size, S_{21}, and design simplicity, but the strip dipole models exhibit the widest bandwidth and highest peak gain, while only being slightly larger in structure. Two strip dipole test antennas were constructed and the S_{11} was measured. The measured results of the fabricated antennas agree with the simulation predictions.

1.3 Roadmap

In addition to size and weight comparisons, the antennas are also compared by their fractional bandwidth and peak gain. Additionally the coupling between the transmit and receive antennas is considered and quantified by the S_{21} of the bi-static system. The fractional bandwidth and gain, along with other antenna and radar specific theory, are explained in Chapter 2.

The wire and strip dipole, designs and their results are contained in Chapter 3. The helical antenna design and results are contained in Chapter 4. The triangular, half elliptical and elliptical, and acorn-shaped bowties with their respective results are contained in Chapter 5. Chapter 6 contains the conclusion discussing the best performing antennas, in addition to future work and possible improvements.

2 Theory and Background

2.1 Radar Theory

The radar transmit signal may take the form of a pulse, a continuous wave or an interrupted continuous wave, each with the capabilities to be modulated in frequency. Frequency modulation changes the frequency of the radar signal during a transmission. Although the addition of a frequency modulated signal introduces extra complexity to the system, it can be used to improve the range resolution.

The range of a target is the distance between the target and the radar system. The range resolution is the ability of the radar system to discriminate between two or more targets in the same direction but at different ranges. The smaller the range resolution, the closer the objects can be spaced and still remain distinguishable. For ground penetrating radar, range resolution is an important characteristic as subsurface materials are all spaced closely together and significant detail is lost with low resolution [2].

For a typical, unmodulated pulsed radar, the range resolution (ΔR) is

$$\Delta R = \frac{c}{\tau}, \tag{2.1}$$

where C is the speed of light in a medium and τ is the pulse length. This relationship demonstrates that obtainable range resolution for an unmodulated pulsed radar is limited by the pulse length [3] [4].

For a linear frequency modulated continuous wave radar (LFMCW), the range resolution is determined by the frequency change that occurs over the period of the chirp. This relationship is shown in Equation 2.2

$$\Delta R = \frac{c|\Delta f|}{2\left(\frac{df}{dt}\right)}, \tag{2.2}$$

where Δf is the bandwidth (frequency difference) in Hertz, and $\frac{df}{dt}$ is the frequency shift per unit time. If the time of the chirp is constrained (i.e. due to the "pulse" or chirp length), the range resolution becomes directly dependent on the bandwidth of operation. Therefore a greater bandwidth can produce greater range resolution, so we desire to use the widest possible bandwidth.

2.2 Antenna Theory

An antenna is a device that facilitates the transform between time-varying currents and electromagnetic wave propagation. As a time varying current travels across an antenna it induces a time-varying electric field. The induced electric field then induces a time-varying magnetic field, which induces another electric field. This chain of events creates an electromagnetic wave that propagates away from the antenna.

Similarly, when an electromagnetic wave becomes incident on an antenna, the incoming electric field induces a current in the conducting material of the antenna. Maxwell's equations define a very predictable relationship between induced currents, electric fields, and magnetic fields. As a result, the path a current takes across an antenna allows for an accurate model for the manner in which the antenna radiates.

2.2.1 Radiated Power

The time-averaged radiated power density of an antenna, as a function of the radial distance r, zenith angle θ, and azimuth angle ϕ, can be obtained through

$$\vec{S}(r,\theta,\phi) = \frac{1}{2}Re[\vec{E}(r,\theta,\phi) \times \vec{H}(r,\theta,\phi)^*], \tag{2.3}$$

where $\vec{E}(r)$ and $\vec{H}(r)$ are the electric and magnetic fields radiated by the antenna, evaluated at some point in space. Through the relationship of the $\vec{E}$ and $\vec{H}$ in Maxwell's equations with the constitutive relations, this relationship can be reduced to

$$\vec{S}(r,\theta,\phi) = \frac{|\vec{E}(r,\theta,\phi)|^2}{2\eta}\hat{r}, \tag{2.4}$$

where η is the characteristic impedance of free space and $\hat{r}$ is the unit vector equivalent to the spherical point (θ,ϕ) [5]. By integrating the power density over all directions θ and ϕ, the total power radiated at distance r is

$$P_{rad} = \int_0^{2\pi}\int_0^{\pi} \vec{S}(r,\theta,\phi)\sin\theta d\theta d\phi = \frac{1}{2}|I_0|^2 R_{rad}, \tag{2.5}$$

where I_0 is the input current and R_{rad} is the radiation resistance of the antenna represented as an equivalent transmission line load that dissipates the power that is radiated by the antenna [6].

2.2.2 Directivity and Gain

The directivity of an antenna is an important characteristic that is used to classify the shape of the radiation pattern in reference to a isotropic source. This is calculated by taking the ratio of the radiation density at all points in space to radiation density of an isotropic source

$$D = \frac{\vec{S}(r,\theta,\phi)}{S_{iso}}. \tag{2.6}$$

Although the directivity of an antenna gives useful information regarding how the antenna radiates, it does not account for resistive losses associated with the physical material of the antenna.

The input impedance of an antenna, Z_{in}, can be described by the relationship

$$Z_{in} = R_{Loss} + R_{rad} + jX_A, \tag{2.7}$$

where R_{Loss} represents the resistance associated with dielectric and conduction loss, and X_A represents the reactance associated with the radiated energy [5]. If we model the input impedance as a series of resistances as depicted in Figure 2.1, then we can use a voltage divider to determine how much voltage is dropped across R_{rad}. The percentage of power that is dissipated over R_{rad} is the radiation efficiency

$$\eta_{rad} = \frac{R_{rad}}{R_{rad} + R_{loss}}. \tag{2.8}$$

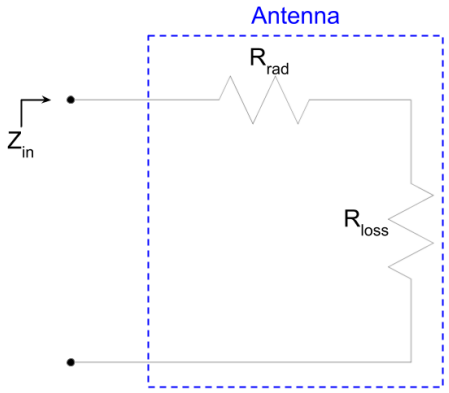

Figure 2.1: Representation of the equivalent circuit input impedance composed of the radiation and loss resistances for a typical antenna.

By scaling the directivity by the radiation efficiency, the gain of the antenna is obtained, which is a characterization of how well the the antenna converts input power into radiation. This relationship is found through

$$G = \eta_{rad} D. \tag{2.9}$$

2.2.3 Impedance Matching

For a transmit antenna to radiate, it must be driven by some type of source with a Thévenin equivalent impedance of R_{src}. To connect the source to the antenna, a transmission line of characteristic impedance Z_c is used. To minimize power loss between the source and transmission line, the transmission line can be chosen so that $Z_c = R_{src}$. This setup is demonstrated in Figure 2.2.

Through basic circuit analysis, it can be shown that the power dissipated across the antenna is maximized when the characteristic impedance of the transmission line matches the input impedance of the antenna. When the characteristic impedance of the transmission line does not match the input impedance of the antenna, voltage reflections occur. This mismatch is

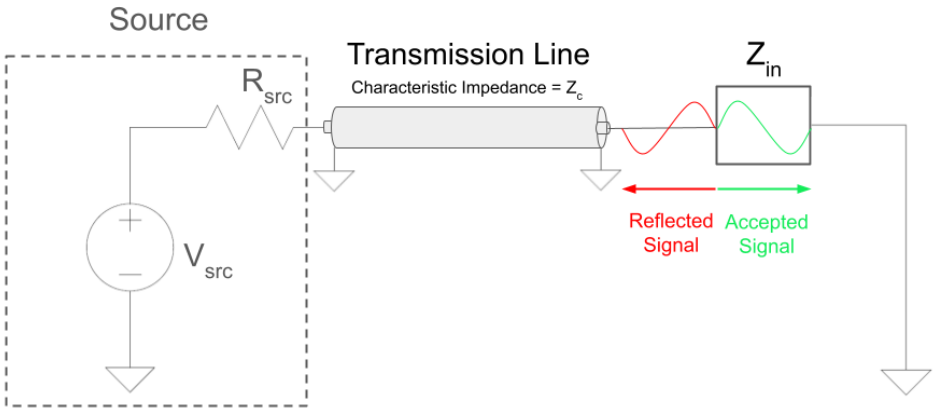

Figure 2.2: This figure shows the circuit equivalent model for a basic antenna setup, where the antenna is modeled as the impedance Z_{in}. The power signal reflected due to an impedance mismatch between the transmission line and the antenna is depicted in red, where as the signal accepted into the antenna is depicted in green.

characterized by the reflection coefficient Γ, which is the ratio of the voltage reflected off the input terminals of the antenna to the voltage traveling in the forward direction. Another name for the reflection coefficient is S_{11}, which is used throughout this paper and found through the relationship

$$S_{11} = \Gamma = \frac{V_{\text{reflected}}}{V_{\text{forward}}} = \frac{Z_{in} - Z_c}{Z_{in} + Z_c}. \tag{2.10}$$

Since the input impedance of the antenna is a function of frequency, as demonstrated by its reactance in (Equation 2.7), it is standard to characterize the antenna as operational at frequencies where the reflection coefficient is below 10 percent or -10 dB. The range of frequencies over which an antenna is operational is called the bandwidth or absolute bandwidth. Additionally, the antenna can be characterized by its fractional bandwidth which is characterized by the absolute bandwidth divided by the center frequency of operation.

To mitigate power loss due to impedance mismatch, a matching network can be added between the transmission line and the input terminals of the antenna. To increase the bandwidth of an antenna, broadband impedance matching techniques may be used; however, these tend to be complicated and are beyond the scope of this research. Instead this research uses antenna models whose input impedance's are less susceptible to changes in frequency. To further improve the S_{11} at the center frequency of operation, narrow band matching circuits are implemented [7]–[9]. These circuits are shown in the design chapters (3-5) of this paper.

A bi-static radar system contains both a transmit and a receive antenna. When energy is radiated from the transmit antenna in a bi-static system, some of it may be captured by the receive antenna instead of being first reflected off the target, which is at greater distance than the spacing between the transmit and receive antennas.

The S_{21} is a measurement of the amount of power that is received at the receive terminal (Rx port) in reference to the power injected into the system by the source at the transmit terminal (Tx port). The Tx port connects to the transmit antenna network, which consists of the transmit antenna and its matching network. The Rx port connects to the receive antenna network, which consists of the receive antenna and its matching network. A block diagram of the S_{21} measurement configuration and the orientation of the transmit and receive antennas are displayed in Figure 2.3. From the S_{21} measurement, the transmit-to-receive isolation in dB is obtained through

$$\text{Isolation (dB)} = -20\log_{10}(|S_{21}|). \tag{2.11}$$

The S_{21} calculations in this Thesis consist of simulations where the transmit and receive antennas are identical models. For this measurement, the transmit and receive antennas are oriented in tandem length-wise and separated by 600 mm.

2.3 Antenna Designs

Through changing the shape, size, and materials of an antenna, different characteristics can be achieved. This section includes basic theory for the three antenna classes considered in this Thesis: dipole antenna, bowtie antenna, helical antenna.

Within the Dipole Antenna subsection, a brief introduction to the half-wavelength wire dipole is given, along with basic justifications for the use of a strip dipole. Within the Bowtie Antenna subsection, the triangular, elliptical, and half elliptical bowtie antennas are introduced as lightweight models with the potential to obtain wider bandwidth than a thin wire dipole. In the Helical Antenna subsection, basic design constraints for a helical antenna in axial mode are given.

2.3.1 Dipole Antenna

One of the most basic types of antennas is the half-wavelength dipole. A half-wavelength dipole antenna can be best understood by analyzing how a time-varying current travels across a thin, lossless wire of finite length. As a time-varying current travels across the wire conductors of a dipole antenna, it inevitably encounters the end of the conductor. When the time-varying current meets the end the current is reflected and undergoes a 180 degree phase shift that propagates in the opposite direction as the incident current. Since the reflected current is traveling in the opposite direction as the incident current, we can model the combined currents together as a standing wave (see Figure 2.4).

When the length of a dipole is approximately half a wavelength of the frequency of operation, the resultant standing wave becomes in phase with the incident current and the input reactance becomes zero. This produces a current distribution with the current at a maximum at the input terminals. In contrast, as the length of a dipole becomes close to a full wavelength, the input impedance of the antenna becomes infinite as the current distribution

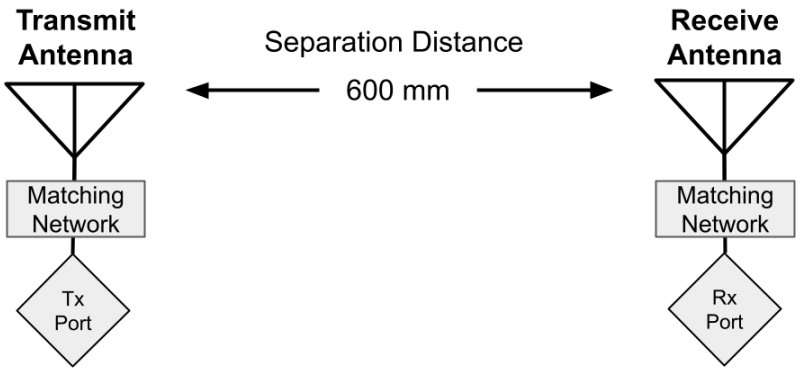

(a) Diagram of S_{21} measurement.

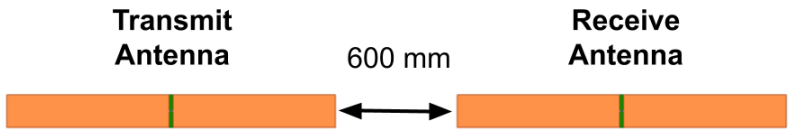

(b) The end-to-end orientation of the transmit and receive antennas for the S_{21} measurement. Strip dipoles are used as the example antennas.

Figure 2.3: The orientation diagrams of the S_{21} measurement.

approaches zero at the terminals [8], [10]. These current distributions of the half and full wave length dipoles are displayed in Figure 2.4.

Dipoles are a type of resonant antenna, meaning that when they operate at their resonant frequency their input reactance becomes zero. At resonance, simple half-wave dipoles are very efficient; however, they generally do not have wide operational bandwidth because of the standing wave currents [11]. It has been proposed that wider bandwidth can be achieved by decreasing the length-to-diameter ratio of the dipole because this lowers the sensitivity of the impedance as a function of frequency [5]. This method may not be practical for lightweight applications limited in space, especially at low frequencies. Instead, a strip dipole antenna can be used which maintains a similar idea but the two arms of the dipole are printed on a substrate instead of a cylindrical wire. An example of a strip dipole antenna is displayed in Figure 2.5.

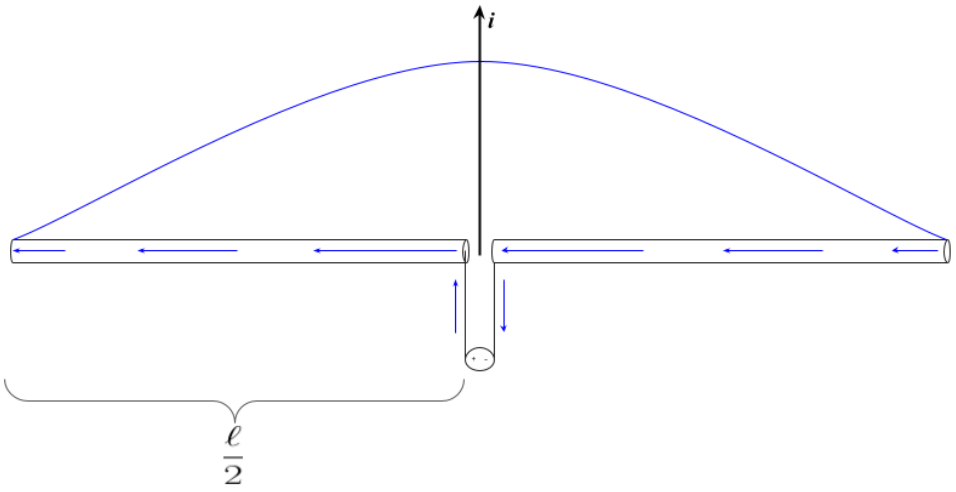

(a) $\ell = \frac{\lambda}{2}$

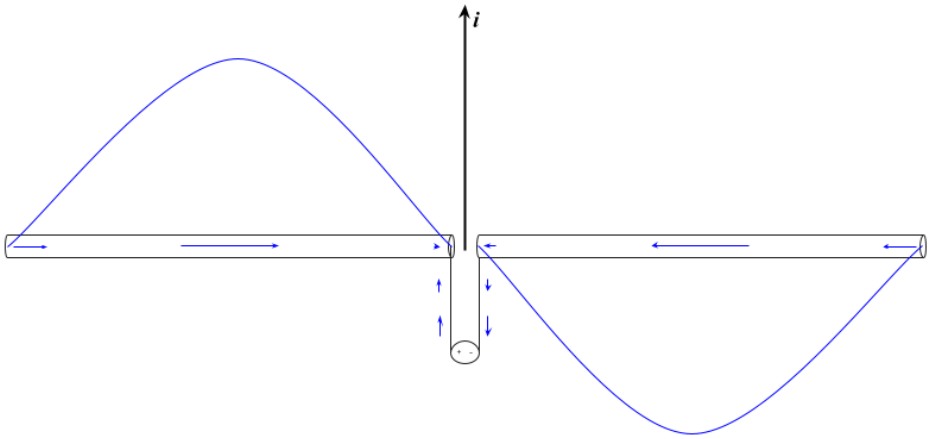

(b) $\ell = \lambda$

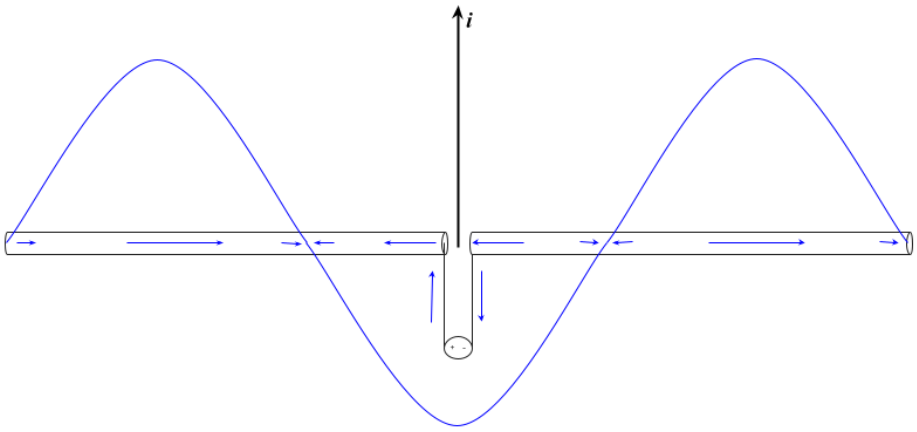

(c) $\ell = \frac{3\lambda}{2}$

Figure 2.4: Standing wave current superimposed over a wire dipole antenna, where the current axis is represented with the black arrow labeled i.

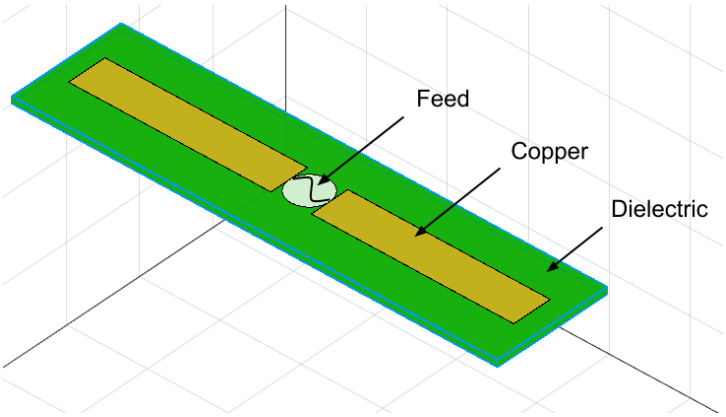

Figure 2.5: The basic structure of the strip dipole antenna.

2.3.2 Bowtie Antenna

Upon the search to increase the bandwidth of an antenna, the biconical antenna was produced [12]. The biconical antenna is similar to wire dipole, but the conductors are flared out at an angle α to produce a cone-like structure exhibited in Figure 2.6. As the flare angle increases, the input impedance decreases along with its sensitivity to changes in frequency [5].

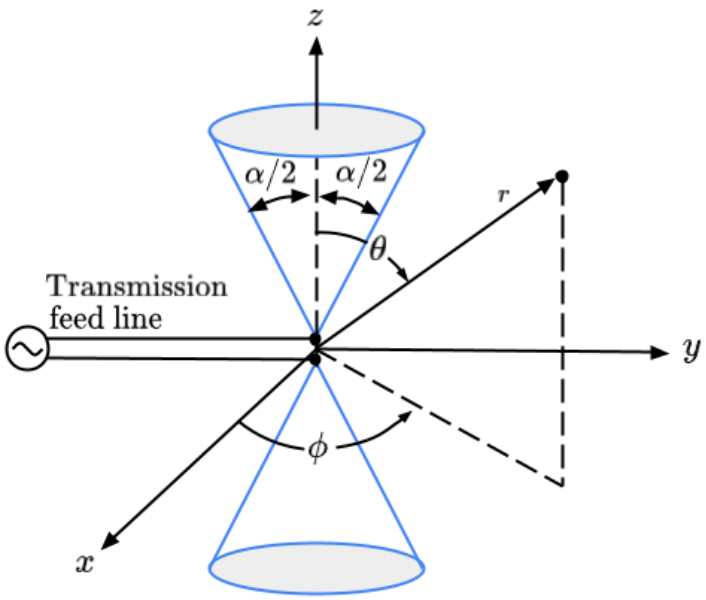

Figure 2.6: The basic structure of a biconical antenna.

When a time-varying voltage is applied at the input terminals, current flows along the surface of the cones and the antenna structure behaves similar to that of a uniformly tapered transmission line [5]. If the cones have infinite length, there are no current reflections off the end, which eliminates

standing waves, and produces broadband characteristics [13].

A finite length biconical antenna may still produce broadband characteristics, since the reflections off the end of the conductor causes a reduction in the operational bandwidth. In practice, a biconical antenna is not desirable for operation in the VHF and UHF bands because of its size. To reduce the profile, while maintaining some of the broadband characteristics, the bowtie antenna was invented [12].

Similar to the biconical antenna, the triangular bowtie antenna also utilizes flare angle to achieve an increase in bandwidth, but as a small planar version, it can be printed on a substrate. Changing the shape of the conductor to an ellipse or half ellipse can also alter the bandwidth performance by providing smoother paths over which the input current can travel [11]. The addition of rounded edges end of the conductor has also been demonstrated to improve bandwidth characteristics by reducing the effect that current reflections off the end of the antenna have on the frequency sensitivity [14]. Basic representations of triangular, elliptical, and half elliptical bowtie antennas are displayed in Figure 2.7.

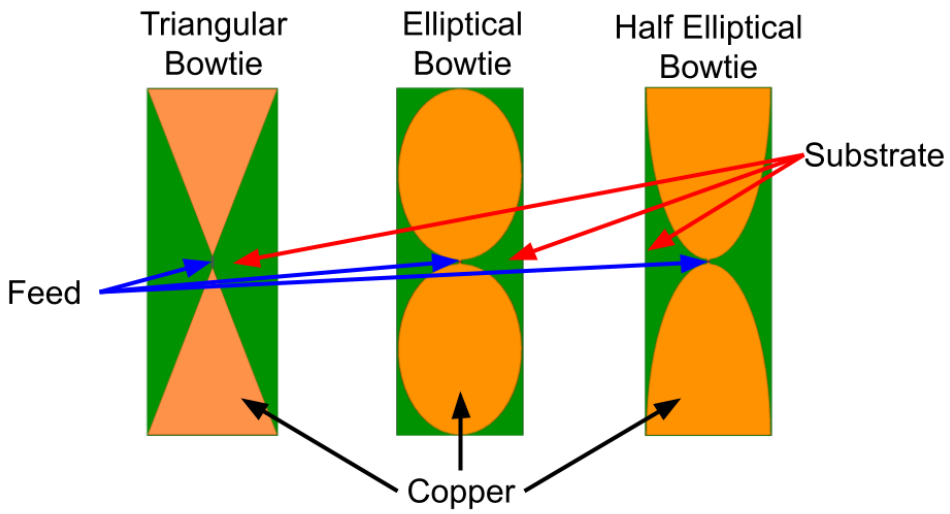

Figure 2.7: Basic geometry of a triangular, elliptical, and half elliptical bowtie antennas.

2.3.3 Helical Antenna

Helical antennas are desirable in many wireless communication applications because of their wide operational bandwidth, and high gain (in axial mode). They are not generally considered for small airborne applications because their relatively large structure; however, it is included in this research upon request from an advisor.

A helical antenna is a type of traveling wave antenna constructed by winding a conductor (wire) in the form of a helix. At the base of the helix, ground planes are commonly used as reflectors with a diameter that is at least $\lambda/2$ [5], [15]. The spacing between each turn, denoted as S, is calculated

from the pitch angle, α

$$S = \pi D \tan(\alpha), \tag{2.12}$$

where D is the diameter of the helix. A diagram for the basic structure of a helical antenna is shown in Figure 2.8.

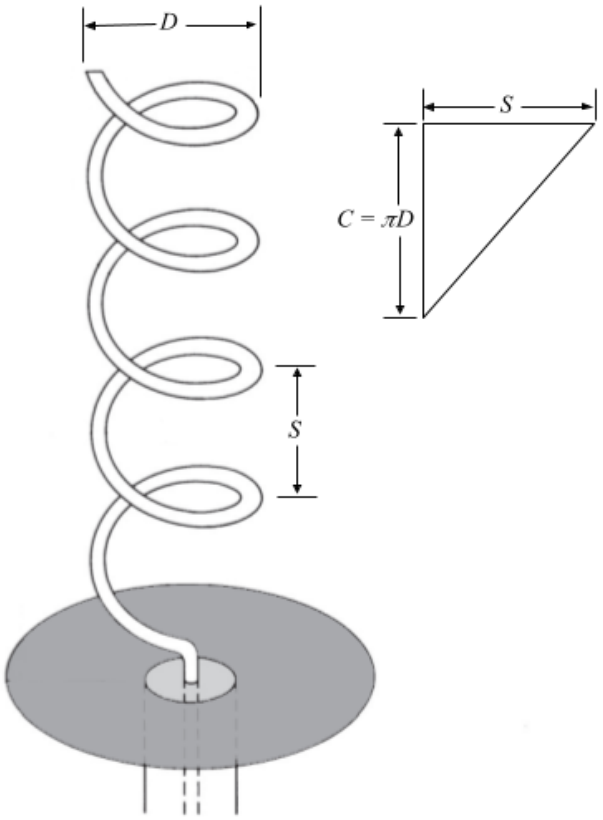

Figure 2.8: The basic geometry of a helical antenna, where D is the diameter of the helix, S is the distance between each loop, and C is the circumference, adapted from [5].

By varying the diameter in relation to the wavelength of the frequency of operation, the helical antenna can be chosen to operate in one of three modes: normal mode, conical mode, or axial mode [5][8]. The helical antenna operates in normal mode when the circumference of the helix, C, is less than $\frac{3}{4}\lambda$. Normal mode produces a semi-omnidirectional pattern orthogonal to the direction in which the helix extends. Conical mode is achieved when C is greater than $\frac{5\lambda}{4}$. This mode produces two main lobes at an angle with a small side lobe in the broadside direction. Axial mode is achieved when $\frac{3\lambda}{4} < C < \frac{4\lambda}{3}$, which produces a single main lobe along the axis of the helix [16]. For example, if the circumference of the helix is equal to the wavelength of a 300 MHz signal (1 m), then the helical antenna maintains operation in axial mode from approximately 225 MHz to 400 MHz. Examples of the three main modes of a helical antenna and their radiation patterns are displayed in Figure 2.9.

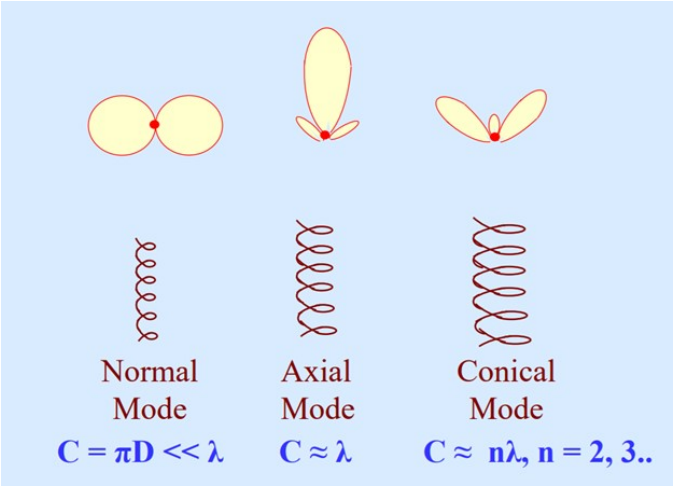

Figure 2.9: Three main modes of the helical antenna. [17]

3 Dipole Antenna Designs

In this chapter, a brief simulation analysis and comparison is done on wire and strip dipole models, which are designed and simulated with Ansys high-frequency structure simulator (HFSS). Additionally, a strip dipole prototype is fabricated and measured to validate the S_{11} of its corresponding simulated model.

The wire dipole model is constructed by placing a feed between two copper cylinders, oriented with their ends facing each other. The wire dipole is included to provide basic comparison data; it is not optimized for performance and only minor design decisions were used to make it operational from 225 MHz to 255 MHz.

The strip dipole model is constructed in a similar manner as the wire dipole, but with rectangular copper sheets printed on FR4-Epoxy PC board in place of cylinders. A brief parameter study is conducted on the effects of changing the length and width of the copper sheets. The size, weight, -10 dB bandwidth, max gain, and transmit-to-receive isolation (see Chapter 2) of the different models are collected for comparison.

3.1 Wire Dipole

The wire dipole antenna is designed to have a total length of approximately 600 mm and a diameter of 3.264 mm, which is the diameter of 8 AWG wire. The antenna is calculated to weight approximately 0.09 lbs plus the weight of the mounting material. The antenna geometry is displayed in Figure 3.1.

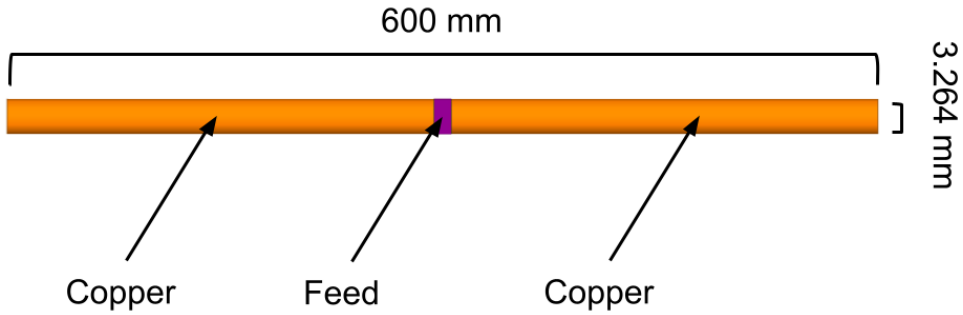

Figure 3.1: The structure of the wire dipole.

The wire dipole is resonant at approximately 235 MHz, with −10 dB bandwidth of 225 MHz to 243 MHz. With the addition of the simple matching network shown in Figure 3.2, the usable bandwidth becomes 224 MHz and 256 MHz. The S_{11} plots for both the matched and unmatched models are displayed in Figure 3.3.

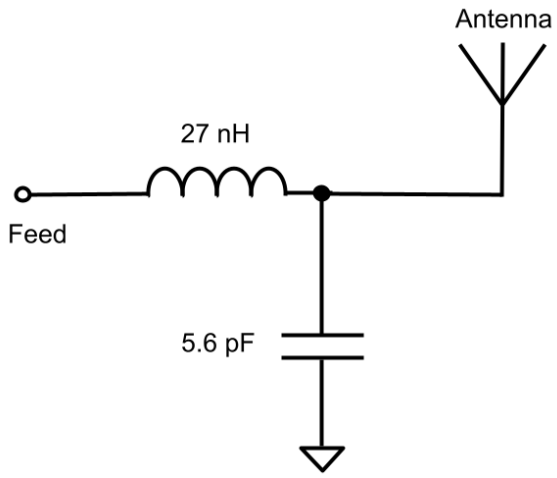

Figure 3.2: The matching network applied to the input terminals of the wire dipole antenna model. The port labeled Feed is where the matching network connects to the 50 Ω transmission line. The port labeled Antenna is where the matching network connects to the antenna.

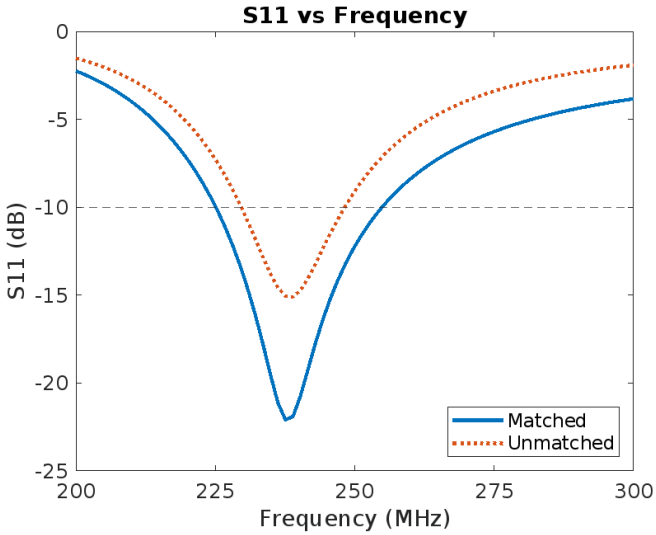

Figure 3.3: The S_{11} vs. frequency plots for the wire dipole simulation. The unmatched solution is displayed with a red dotted line and the matched network is displayed with a blue solid line.

3.2 Strip Dipole

In [18], a brief parameter study is presented on the strip dipole, where the length of each arm is constrained and the width of one of the arms is varied. As the width of the arm increased, the study demonstrated that the antenna bandwidth also increased. I follow a similar process but instead of varying only the width of a single arm (copper sheet), changes are applied to both the length and width of each arm to demonstrate the bandwidth capabilities. The strip dipole is considered at copper sheet widths of 50 mm, 75 mm, and 100 mm with corresponding strip lengths of 260 mm, 255 mm, and 250 mm, respectively. The length of each sheet is chosen to maintain operation at 225 MHz. As the width of the copper increases, there is a general increase in the bandwidth on both sides of the center frequency. This allows the wider models to be operational at 225 MHz with shorter lengths.

The rectangular sheets are spaced 6 mm apart and small stubs, 1.75 mm in width, are added on the inside as a connection point for the source. The copper sheets are backed by an FR4-Epoxy substrate that maintains a 1 mm barrier surrounding the outside of the copper sheets. This produces total lengths of 528 mm, 518 mm, and 508 mm. The calculated weight for the 50 mm, 75 mm and 100 mm widths, not including mounting hardware, are 0.17 lbs, 0.22 lbs, and 0.27 lbs, respectively. The basic structure of the strip dipole model is displayed in Figure 3.4.

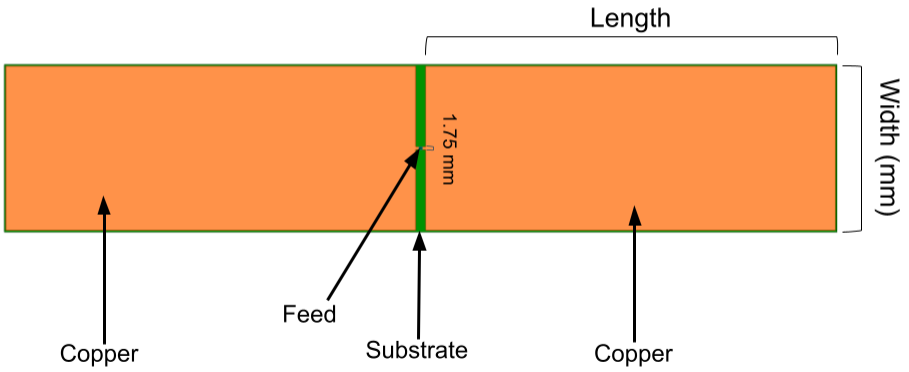

Figure 3.4: The structure of the strip dipole.

The width of the strip dipole has a significant effect on the operational bandwidth. For sheet widths of 50 mm, 75 mm, and 100 mm, the −10 dB bandwidth is 36 MHz, 44 MHz, and 56 MHz, respectively. With the addition of simple matching networks, the bandwidths for widths of the 50 mm, 75 mm, and 100 mm lengths are increased to 58 MHz (225 MHz – 283 MHz), 62 MHz (225 MHz – 287 MHz), and 78 MHz (225 MHz – 303 MHz), respectively. The S_{11} versus frequency plots and the matching networks for each simulated configuration are displayed in Figure 3.5.

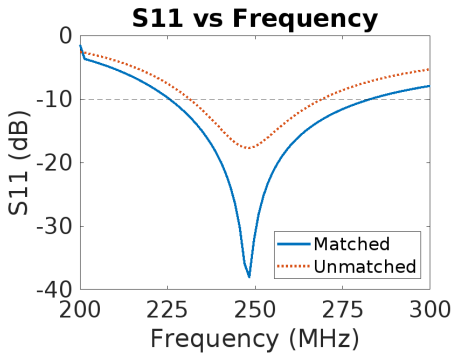

(a) S_{11} vs. frequency
width = 50 mm
length = 260 mm

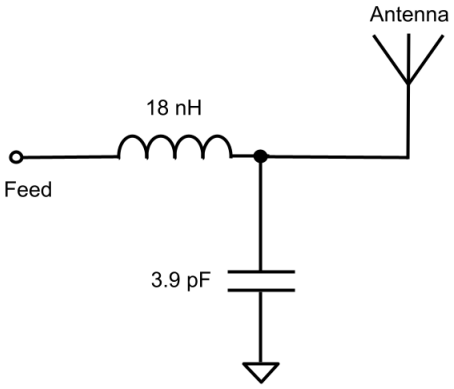

(b) Matching network
width = 50 mm
length = 260 mm

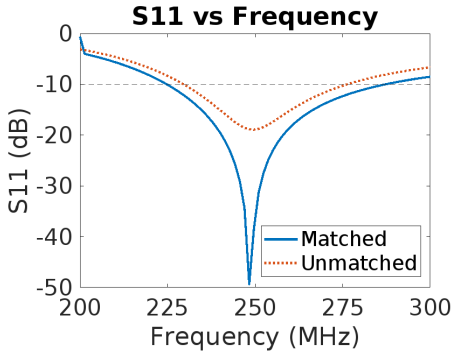

(c) S_{11} vs. frequency
width = 75 mm
length = 255 mm

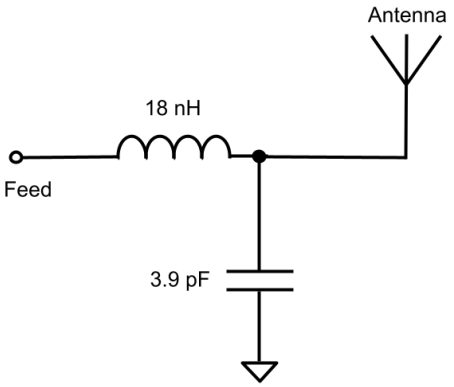

(d) Matching network
width = 75 mm
length = 255 mm

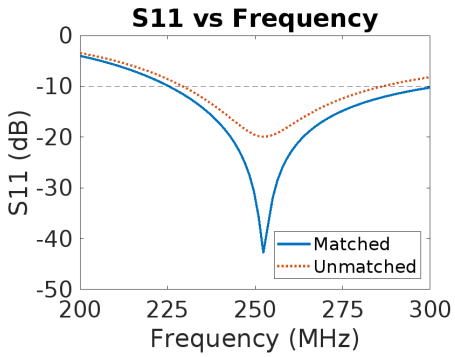

(e) S_{11} vs. frequency
width = 100 mm
length = 250 mm

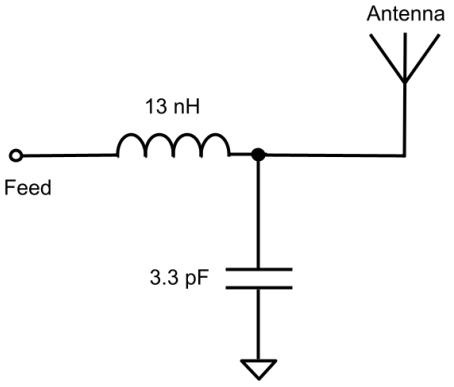

(f) Matching network
width = 100 mm
length = 250 mm

Figure 3.5: The S_{11} vs. frequency plots for the simulated matched and unmatched strip dipole models of different sizes. The matching network configurations are included to the right of their corresponding plot.

3.3 Comparison

In this section, several dipole models are compared by operational bandwidth, peak gain, and the isolation between the transmit and receive antennas with a separation distance of 600 mm. Comparison plots are provided.

Upon examination of the −10 dB bandwidth performance in Figure 3.6, it can be seen that the strip dipole models out perform the wire dipole in obtainable bandwidth. This difference is accentuated further as the width of the strip dipole conductor increases, at least until the strip gets too wide.

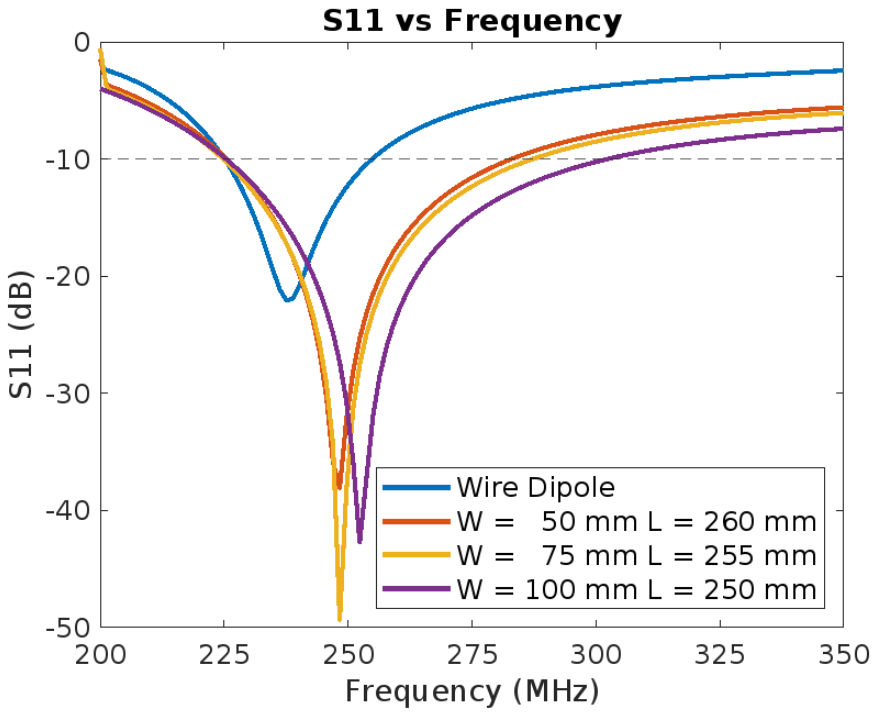

Figure 3.6: The S11 vs. frequency plots for the simulated wire dipole and strip dipole for sheet widths of 50 mm, 75 mm, and 100 mm, where W is the width of the strip and L is the length of the strip.

The wire and strip dipole models exhibit similar isolation behavior. Each model has a peak in their respective S_{21} response at the lower end of their band of operation. As the frequency increases, the isolation increases.

Over their respective band of operation, the wire dipole model exhibits the most transmit-to-receive isolation (lowestS_{21}) out of the four models. The minimum isolation for the wire dipole is 29 dB at 225 MHz and the maximum is 33 dB at 255 MHz. Out of the strip dipole models, the 50 mm width has the most isolation with a minimum of 28 dB at 230 MHz and a maximum of 34 dB at 282 MHz. The next best isolation is achieved by the 75 mm width model, which obtains a minimum of 28 dB at 227 MHz and a maximum of 34 dB at 287 MHz. The 100 mm width strip dipole model

exhibits the least amount of isolation with a minimum of 27 dB at 228 MHz and a maximum of 33 dB at 303 MHz.

Over the GPR operational range (225 MHz to 255 MHz), the maximum isolation of the 50 mm width model is 30 dB, the maximum isolation for the 75 mm width model is 29 dB, and the maximum isolation for the 100 mm width model 28 dB. Over the GPR band, the maximum isolation for all three strip dipole models occur at 255 MHz. The S_{21} versus frequency plots are displayed in Figure 3.7.

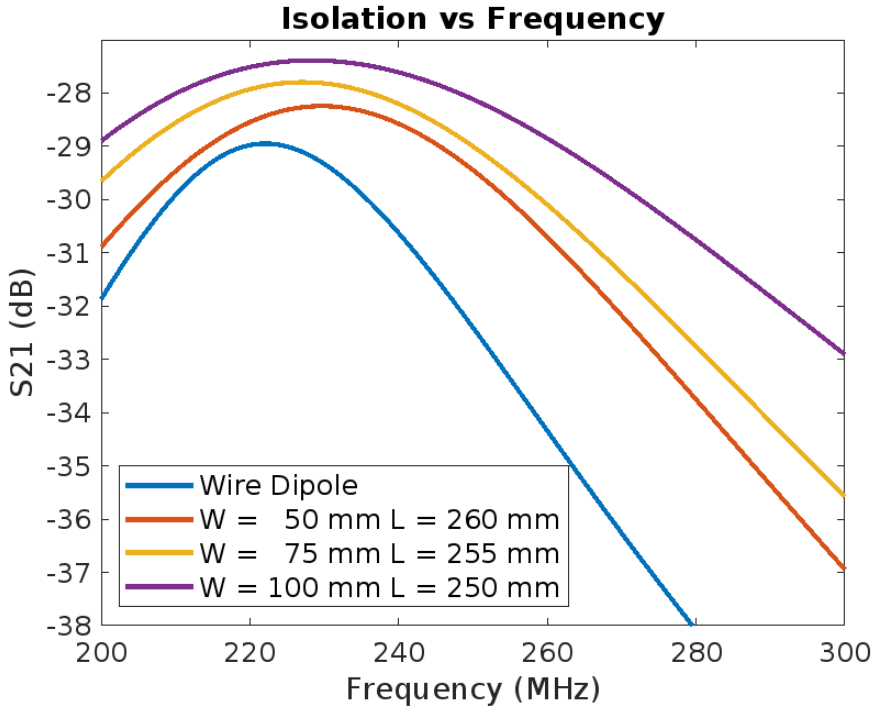

Figure 3.7: The S_{21} vs frequency plots for the simulated wire dipole and strip dipole for sheet widths of 50 mm, 75 mm, and 100 mm.

The peak gain for the dipole models over the frequency range at which the GPR will operate are between 2.1 dB and 2.15 dB. The 100 mm width strip dipole model exhibits the highest peak gain, followed by the 75 mm width strip dipole, the 50 mm width strip dipole, and then the wire dipole. The peak gain vs. frequency is plotted for the considered models in Figure 3.8. The radiation pattern of the strip dipole models exhibit a slightly higher gain in the broadside direction. This becomes more apparent as the strip width increases from 50 mm to 100 mm. This is illustrated in Figure 3.9, where an azimuth slice of the total gain at 250 MHz is plotted in reference to the strip dipole geometry. From the total gain plot, the gain at can differ by up to 0.15 dB between zenith angles of 0 and 90 degrees. A table containing a summary of the simulated results is available in Table 3.1.

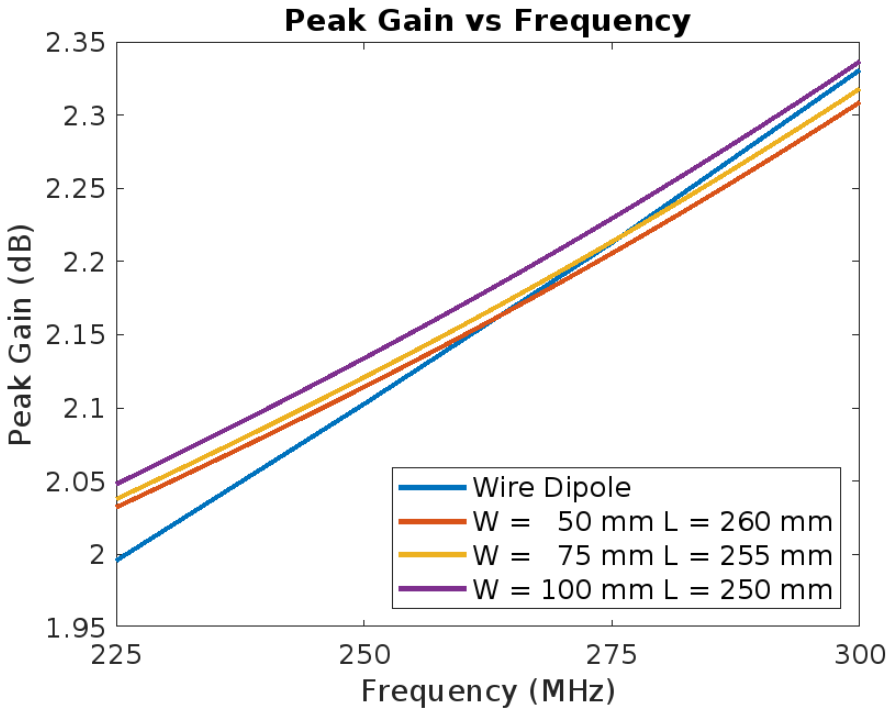

Figure 3.8: The peak gain vs. frequency plots for the wire and strip dipole model simulations, where W is the width of the strip and L is the length of the strip.

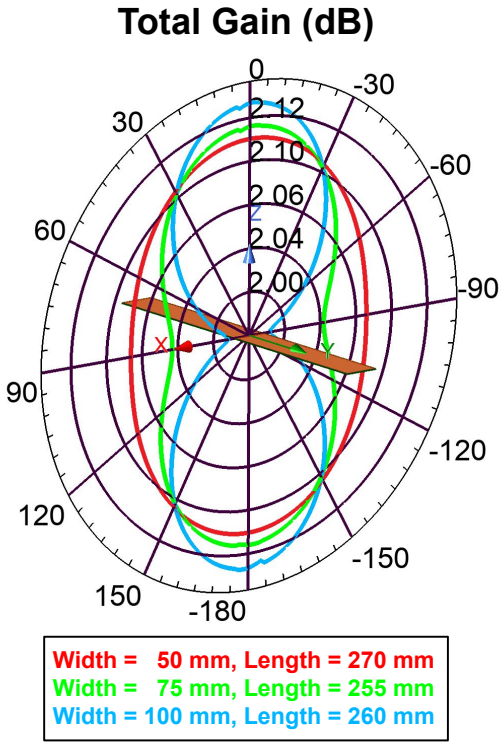

Figure 3.9: The total gain (dB) vs. zenith angle (degrees) at 250 MHz for the 50 mm, 75 mm, and 100 mm width model simulations. The total gain is plotted as a field overlay to give context of the orientation of the strip dipole models.

Table 3.1: The results for the wire and strip dipole simulations. The weight calculations do not include any mounting structure. The minimum isolation, maximum isolation, and maximum gain are calculated over the range in which the GPR will operate (225 MHz to 255 MHz).

Model	Dimensions (mm)	Weight (lbs)	Absolute Bandwidth (MHz)	Fractional Bandwidth (%)	Min Isolation (dB)	Max Isolation (dB)	Max Gain (dB)
Wire Dipole	600 x 3.264 x 3.264*	0.09	32	13.3	29	33	2.11
Strip Dipole	528 x 52 x 1	0.17	58	22.8	28	30	2.13
	518 x 77 x 1	0.22	62	24.2	27	29	2.14
	508 x 102 x 1	0.27	78	29.5	27	28	2.15

* Diameter of 8 AWG wire

3.4 Constructed Model

A physical strip dipole model of 50 mm width is constructed to validate the simulation data. The actual dimensions of the constructed model vary from the models that were simulated earlier in this chapter due to human error. As a result, a new HFSS model is produced to better match the dimensions of the built design. The model is constructed with materials that are easily accessible. The arms of the antenna are constructed by cutting single sided 1 oz copper PCB. The substrate is approximately 1.68 mm thick FR4-Epoxy and approximately 270 mm long. The arms of the antenna are hot glued to thin particle board, and an RG-58 coax cable is soldered onto the copper. The built models are displayed in Figure 3.10. The two constructed models are measured through the process described in Appendix A, and the S_{11} versus frequency plots for the constructed and simulated models are displayed in Figure 3.11.

Figure 3.10: The constructed strip dipole models, where Antenna 1 is on the top and Antenna 2 is on the bottom.

The S_{11} responses for the fabricated antennas share similar characteristics with each other and the simulated model. The−10 dB bandwidth of Antenna 1 is measured to span 212 MHz to 264 (52 MHz), with a center frequency of 238 MHz. Antenna 2 is measured to span 212 MHz to 263 MHz (51 MHz), with a center frequency of 237.5 MHz. The simulation spans 221 MHz to 255 MHz (34 MHz), with a center frequency of 238 MHz. The minimum S_{11} for Fabricated Antenna 1, Fabricated Antenna 2, and the simulation are −18 dB, −22 dB, and −17 dB, respectively.

The major difference between the S_{11} of the constructed antennas and the S_{11} of the simulation is the operational bandwidth. Both fabricated antennas have a significantly wider bandwidth than the simulation, even though the center frequencies only differ from the simulation by less than 1 MHz. From 225 MHz to 255 MHz, Fabricated Antenna 1 matches the simulated S_{11} fairly close; however, Fabricated Antenna 2 reaches significantly lower values than both Fabricated Antenna 1 and the simulation.

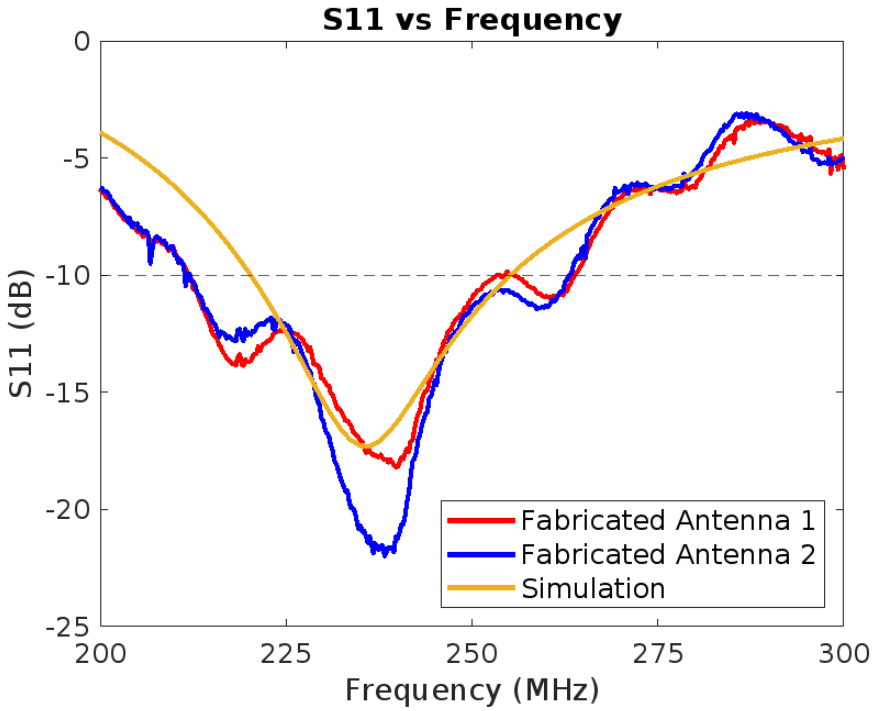

Figure 3.11: S_{11} vs. frequency for the two fabricated strip dipole antennas and the HFSS simulation data.

For being crudely made with easily accessible materials, the S_{11} of the fabricated strip dipole antennas matches fairly well with the simulation. There are some obvious differences between the measured and simulation results which are attributed to human error in the construction of the model, and the method and environment in which the antennas were measured. The measured results are close enough to the simulation that Antennas 1 and 2 can be deemed functional prototypes. To obtain more accurate results, it would be necessary to have the antennas printed and cut professionally.

3.5 Summary

All models in this section meet the 30 MHz bandwidth specifications and could be used for our application. The wire dipole is the smallest and most light weight model, and compares well to the others in maximum gain. It maintains better isolation than the other models and can potentially be the most lightweight. Based upon weight constraint, the wire dipole is the best suited for this application. However, for applications requiring wider bandwidth, the strip dipole should be implemented. A simple adjustment in the width of the strip dipole can be implemented to change the bandwidth characteristics. A similar approach could be done with a wire dipole, but changing the width of a strip dipole is simpler with current PCB printing technology. Overall, the strip dipole is the more versatile option because its ability to maintain wide-band functionality.

4 Wire Helical Antenna Design

In this chapter, a brief simulation analysis is done for a monofilar wire helical antenna, which is designed and simulated with Ansys high-frequency structure simulator (HFSS). Because the simulated model is too big for our application, a physical model is not constructed.

The model is excited through a coaxial feed whose inner conductor connects to the bottom of the helix and the outer conductor connects to the the ground plane. In [19], various ground plane configurations were considered to maximize the directivity and efficiency. Additionally, helical antenna design with a low number of turns is discussed in [20]–[22], along with other considered optimizations. The model in this section is implemented with three different sized circular ground planes to demonstrate the effects on the gain and the isolation. The helical antenna is designed with a center frequency higher than our desired band of operation. This allows for the antenna to be more compact, while still being operable at 225 MHz because of its wide-band characteristics. A simple circuit is used to match the wire helix to a 50 ohm transmission line.

4.1 Design

The circumference of the wire is chosen to be 1 m, which allows the antenna to operate in axial mode from 225 MHz ($4/3\lambda$) to 400 MHz ($3/4\lambda$). The helix is designed with N = 3.5 turns because this produces a relatively constant input impedance over the band at which the GPR will operate. The helix is designed with 8 American Wire Gauge (AWG) solid copper wire with a pitch angle of 12 degrees, which makes the total height of the antenna approximately 750 mm. This size wire is chosen because it is readily available to make a prototype. In [5], it is suggested that the diameter of the ground plane for a helical antenna be at least $\lambda/2$ of the center frequency, with 0.75λ being the preferred length. Since the ground plane is a main contributing factor to the overall size of the antenna, various circular ground plane with diameters of 500 mm (0.5λ), 600 mm ($.6\lambda$), and 750 mm (0.75λ) are considered.

The ground planes are designed to be 1 mm thick aluminum and no structure is added to support the wire helix. The top of the ground plane is covered with 1 mm thick FR4-Epoxy. The total calculated weights for the the 500 mm, 600 mm, and 750 mm diameter ground planes are 6.6 lbs, 5.0 lbs, and 4.2 lbs, respectively. The structure of the helical antenna is displayed in Figure 4.1.

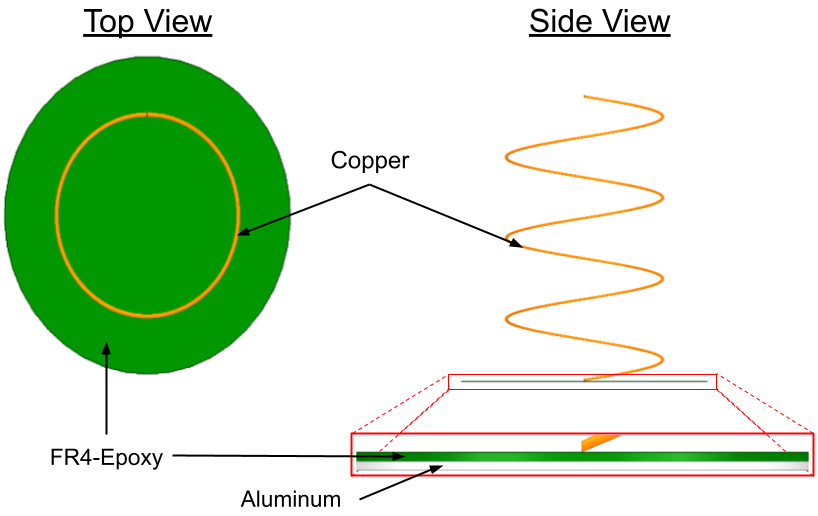

Figure 4.1: The structure of the wire helical antenna design. On the left, an overhead view is displayed. On the right, a side view is shown with an enlarged view of the substrate and ground plane signified with a red box.

Since helical antennas in axial mode typically have an input impedance between 100 and 200 ohms, various techniques (1/4 wave transformer, tapered micro-strip feed, etc.) have been used to lower the input impedance to better match a lower impedance feed [5]. To simplify the geometry, a simple circuit matching network is used (see Figure 4.2). Changing the size of the ground plane only causes minor variations to the impedance response; therefore, the same matching network is used for all three variations.

4.2 Results

The antennas performed similarly with regard to their operational bandwidth. All three variations are operational from approximately 220 MHz to 310 MHz. The S_{11} plots for all three matched ground plane variations are shown in Figure 4.3. The transmit-to-receive isolation of the wire helical antenna is simulated with the three different ground plane sizes through the process described in 3. The S_{21} versus frequency plot for the wire helical antennas are displayed in Figure 4.4.

The three S_{21} plots demonstrate similar behavior. Each exhibits a local maximum between 210 MHz and 230 MHz, decreases to their respective absolute minimum, then begins to rise toward the upper end of their band of operation. The minimum isolation for the ground plane radius of 250 mm is approximately 28 dB at 225 MHz and the maximum is 46 dB at 300 MHz. The minimum isolation for the ground plane radius of 300 mm is approximately 32 db at 227 MHz and the maximum is 38 dB at 290 MHz. The minimum isolation for the ground plane radius of 375 mm is approximately 33 dB at 310 MHz and the maximum is 42 dB at 240 MHz.

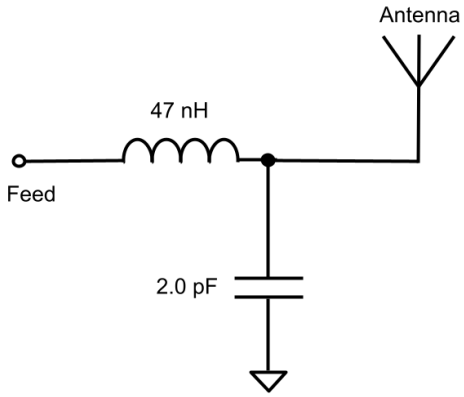

Figure 4.2: The matching network for the wire helical antenna.

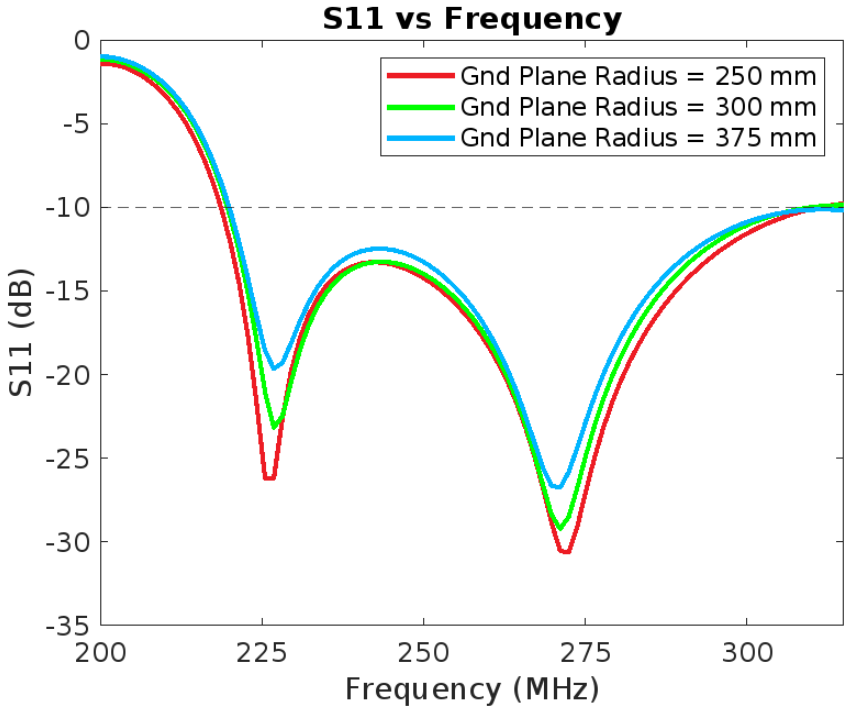

Figure 4.3: The S_{11} vs. frequency plot for the simulated wire helical antenna with ground plane diameters of 500 mm, 600 mm, and 750 mm, with the applied matching network displayed in Figure 4.2.

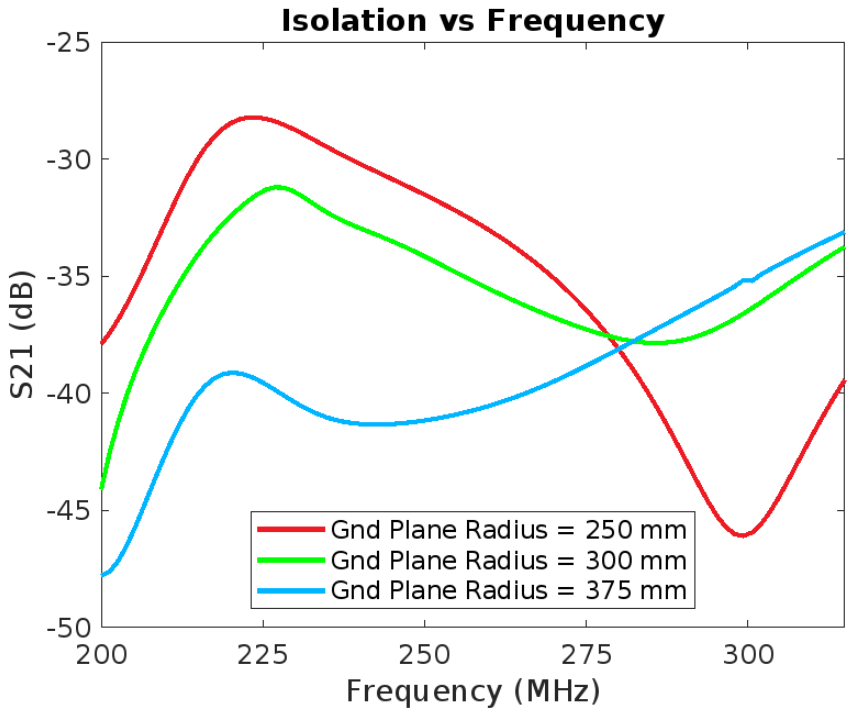

Figure 4.4: The S_{21} vs. frequency plot for the simulated wire helical antenna with ground plane diameters of 500 mm, 600 mm, and 750 mm.

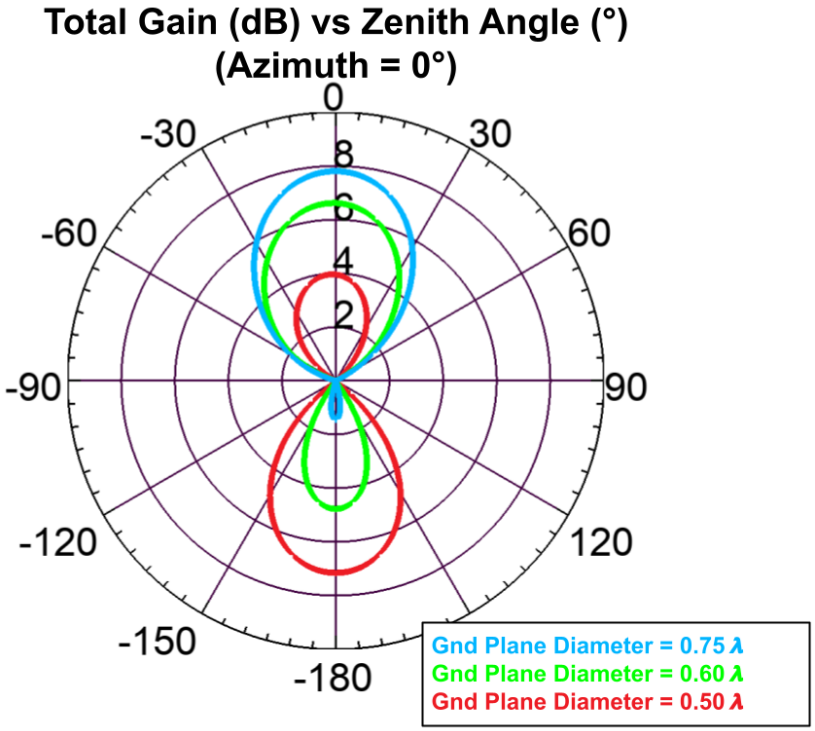

Figure 4.5: The total gain vs. zenith angle in degrees at 250 MHz for azimuth angle of 0 degrees for the simulated wire helical antenna with ground plane diameters of 500 mm, 600 mm, and 750 mm.

From Figure 4.5, it can be seen that the ground plane size has a significant effect on the gain. The model with the ground plane radius of 375 mm achieves the highest gain (8 dB) at 250 MHz in the $\theta = 0$ direction. The next highest is 6.75 dB with the 300 mm radius, then the lowest is 4 dB with a radius of 250 mm. Although the model with the 250 mm ground plane radius exhibits the lowest gain in the $\theta = 0°$ direction, it produces a maximum of 7 dB at $\theta = 180°$.

4.3 Summary

In the band over which the GPR will operate, greater isolation is obtained as the size of the ground plane increases, at least up to a certain point. One of the contributing factors is that an increase in the size of the ground plane results in an increase in the maximum gain in the end-fire direction. As more transmitted radiation is focused away from the receive antenna, it follows that there would be an increase in isolation between the transmit and receive antennas. Even though the wire helical performs well with regard to bandwidth, isolation, and gain characteristics, it is not considered a viable option because of its size and weight. To reduce weight, the substrate could potentially be removed and the solid ground plane could be implemented with a wire mesh, but the width of the antenna and the amount in which the helix protrudes could still be limiting factors. As a result, the helical antenna is not pursued further in this research.

5 Bowtie Antenna Designs

The bowtie antenna has been considered for many GPR applications because of their wideband characteristics [23]–[26]. In this chapter, a brief simulation analysis and comparison is done on simple variations of the triangular, elliptical, and half elliptical bowtie antennas. The antennas are designed and simulated with Ansys high-frequency structure simulator (HFSS). The models are simulated with 1 oz copper printed on 1 mm thick FR4-Epoxy with at least a 1 mm barrier surrounding the outside of the copper. The triangular, elliptical, and half elliptical bowties are designed to have copper widths of 50 mm, 75 mm, and 100 mm.

Additionally, a brief simulation analysis of an acorn-shaped bowtie antenna is added and a prototype is fabricated and measured to validate the S_{11} of simulated model. The size, weight, −10 dB bandwidth, peak gain, and transmit-to-receive isolation (see Chapter 2) of the models are collected for comparison.

5.1 Triangular Bowtie Antenna

The triangular bowtie is considered because it has been demonstrated to show wider bandwidth performance than a wire dipole antenna [13]. In this Thesis, the triangular bowtie consists of two copper isosceles triangles with their inner corners spaced 6 mm apart. The lengths of the triangles are 230 mm, 220 mm, and 210 mm, which correspond to the widths of 50 mm, 75 mm, and 100 mm, respectively. The model is excited at the inner corners of the copper triangles. With the inclusion of the 1 mm barrier and 6 mm spacing, the triangular bowtie model dimensions are 468 mm x 52 mm x 1 mm, 448 mm x 77 mm x 1 mm, and 428 mm x 102 mm x 1 mm, which correspond to calculated weights of 0.16 lbs, 0.20 lbs, and 0.24 lbs, respectively. The basic structure of the triangular bowtie model is displayed in Figure 5.1.

For widths of 50 mm, 75 mm, and 100 mm, the −10 dB bandwidth is approximately 24 MHz (225 MHz to 249 MHz), 27 MHz (225 MHz to 252 MHz), and 31 MHz (225 MHz to 256 MHz), respectively. The addition of a matching network does not significantly improve the bandwidth of the triangular bowtie models and even causes a slight reduction in the bandwidth of the 50 mm and 75 mm width models. The S_{11} vs. frequency plots and the matching networks for each configuration are displayed in Figure 5.2 and all matched S_{11} plots are included in 5.3.

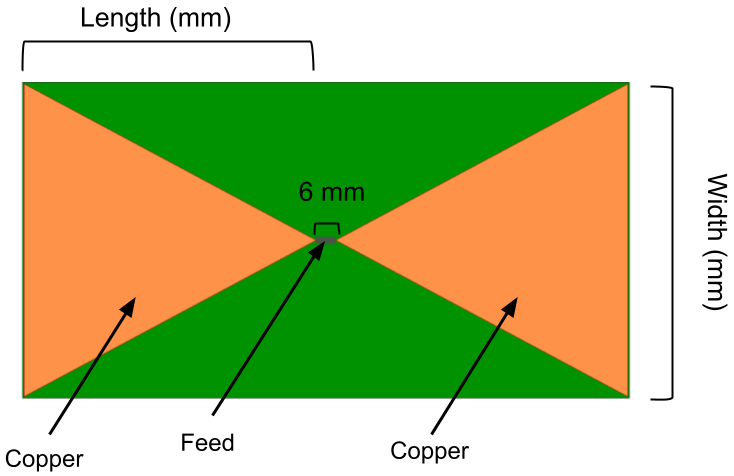

Figure 5.1: The structure of the triangular bowtie model.

The radiation pattern of the triangular bowtie models exhibit a slightly higher gain at broadside than in the end-fire direction. This becomes more apparent as the width increases from 50 mm to 100 mm. This is illustrated in Figure 5.4, where an azimuth slice of the total gain at 250 MHz is plotted as an overlay to the model. In Figure 5.4, the 50 mm model exhibits the highest gain, followed by the 75 mm, then the 100 mm model. From the total gain plot, the difference between the gain at zenith angles 0 and 90 degrees, for all three models, is less than 0.1 dB.

The three triangular bowtie models exhibit similar isolation behavior. Each model has a peak in their respective S_{21} response at the lower end of their band of operation. As the frequency increases, the isolation increases.

Over their respective bands of operation, the 50 mm width triangular bowtie exhibits the most transmit-to-receive isolation (lowest S_{21}) out of the three models (see Figure 5.5); however, the performance of all three models are almost indistinguishable. The 50 mm width has the most isolation, with a minimum of 26 dB at 228 MHz and a maximum of 29 dB at 249 MHz. The next best isolation is achieved by the 75 mm width model, which obtains a minimum isolation of 26 dB at 228 MHz and a maximum of 29 dB at 252 MHz. The 100 mm width model exhibits the least amount of isolation with a minimum 25 dB at 228 MHz and a maximum of 29 dB at 256 MHz.

Since the band at which the GPR operates exceeds the bands at which the 50 mm and 75 mm width triangular bowtie models are operational, the minimum and maximum isolation values described above are the same as the minimum and maximum isolation values over the GPR band. For the 100 mm width triangular bowtie, the maximum isolation over the GPR band is approximately 29 dB at 255 MHz. The S_{21} versus frequency plots for the triangular bowtie models are displayed in Figure 5.5.

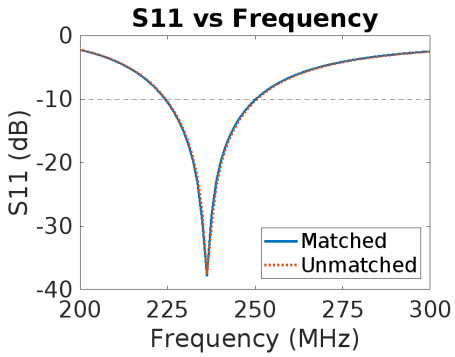

(a) S_{11} vs. frequency
width = 50 mm
length = 248 mm

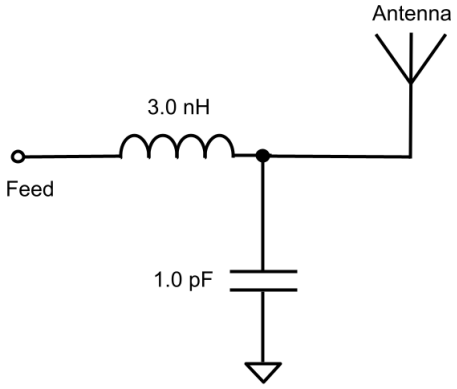

(b) Matching network
width = 50 mm
length = 248 mm

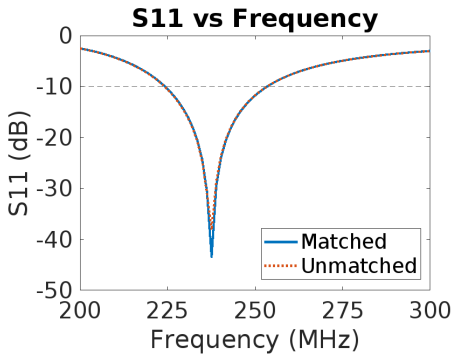

(c) S_{11} vs. frequency
width = 75 mm
length = 240 mm

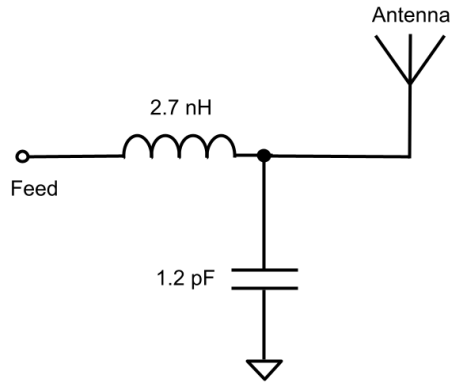

(d) Matching network
width = 75 mm
length = 240 mm

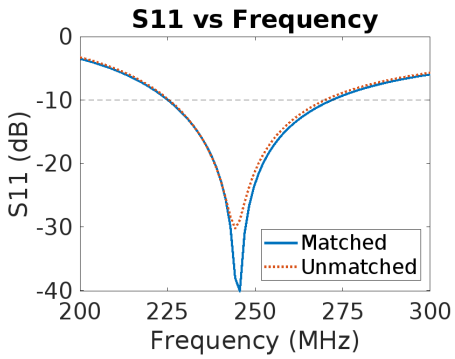

(e) S_{11} vs. frequency
width = 100 mm
length = 231 mm

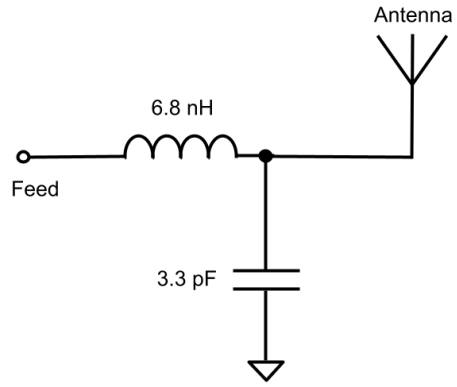

(f) Matching network
width = 100 mm
length = 231 mm

Figure 5.2: The S_{11} vs. frequency plots for the simulated matched and unmatched triangular bowtie models of different sizes. The matching network circuit diagrams are included to the right of their corresponding plots.

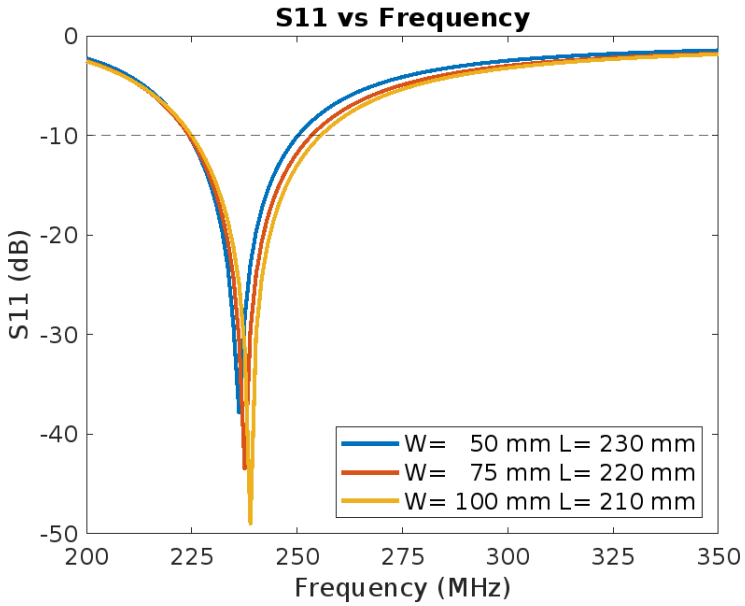

Figure 5.3: The S_{11} vs. frequency plots for the 50 mm, 75 mm, and 100 mm width triangular bowtie models, where W is the width of the triangles and L is the length (height) of the triangles.

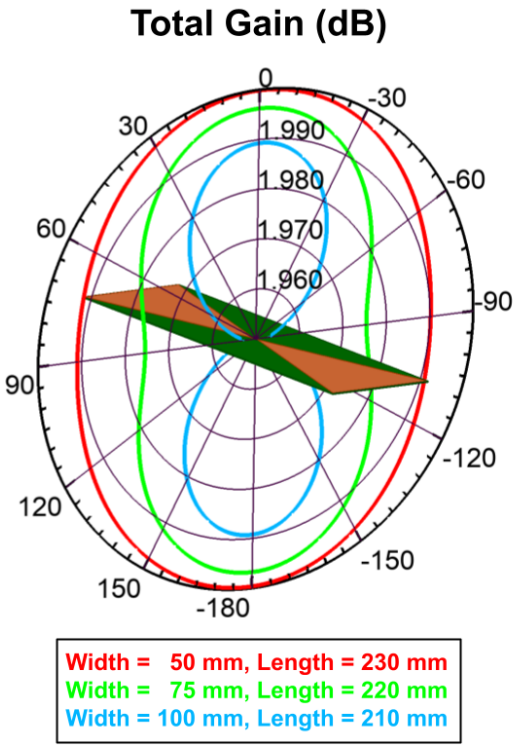

Figure 5.4: The total gain (dB) vs. zenith angle (degrees) at 250 MHz for the 50 mm, 75 mm, and 100 mm width triangular bowtie model simulations. The total gain is plotted as a field overlay to give context of the orientation of the model.

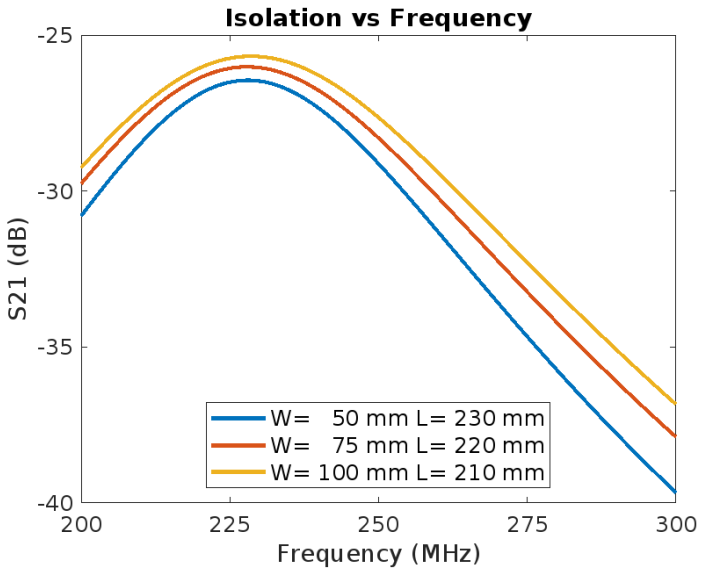

Figure 5.5: The S_{21} vs. frequency plot for the triangular bowtie antenna model simulations, where W is the width of the triangles and L is the length (height) of the triangles.

5.2 Half Elliptical Bowtie Antenna

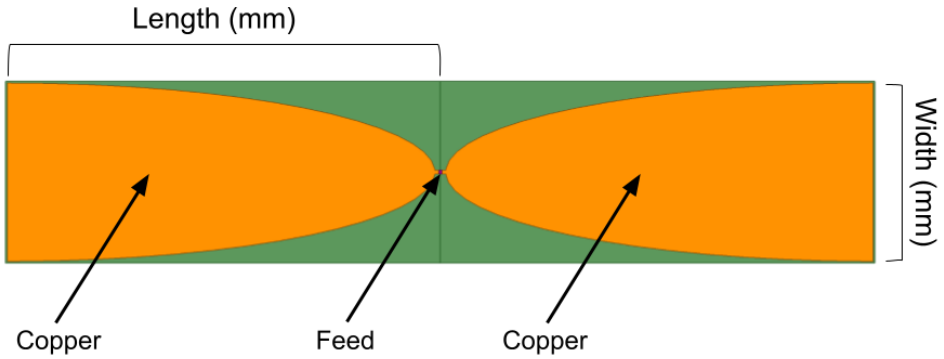

Figure 5.6: The structure of the half elliptical bowtie model.

In [11] and [14], different geometries of the half elliptical bowtie are considered. The half elliptical bowtie antenna is similar in structure to the triangular bowtie, but with half ellipses in place of triangles. The lengths of the half ellipses are 248 mm, 240 mm, and 231 mm, which correspond to widths of 50 mm, 75 mm, and 100 mm, respectively. The half ellipse sheets are spaced 6 mm apart and small stubs (1.75 mm in width), are added on the inside as a connection point for the source. With the inclusion of the 1 mm boundaries and 6 mm spacing, the half elliptical bowtie model dimensions are 504 mm x 52 mm x 1 mm, 488 mm x 77 mm x 1 mm, and 470 mm x 102 mm x 1 mm, which correspond to calculated weights of 0.17 lbs, 0.21 lbs, and 0.25 lbs, respectively. The basic structure of the half elliptical bowtie model is displayed in Figure 5.6.

For widths of 50 mm, 75 mm, and 100 mm, the −10 dB bandwidth is 31 MHz (227 MHz to 258 MHz), 37 MHz (226 MHz to 263 MHz), and 44 MHz (226 MHz to 270 MHz), respectively. With the addition of simple matching networks the bandwidth of the 50 mm, 75 mm, and 100 mm width models increase to 35 MHz (225 MHz to 260 MHz), 42 MHz (225 MHz to 267 MHz), and 46 MHz (225 MHz to 271 MHz), respectively. The S_{11} vs. frequency plots and the matching networks for the simulated configurations of the half elliptical bowtie antennas are displayed in Figure 5.8. All three matched S_{11} plots are in 5.9.

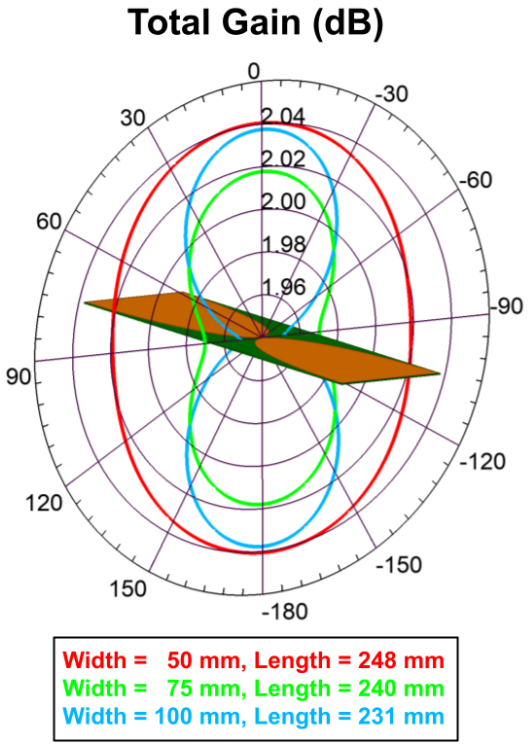

Figure 5.7: The total gain (dB) vs. zenith angle (degrees) at 250 MHz for the 50 mm, 75 mm, and 100 mm width half elliptical bowtie model simulations. The total gain is plotted as a field overlay to give context of the orientation of the model.

Similar to the triangular bowties, the radiation pattern of the half elliptical models exhibit higher gain in the broadside direction. The difference between the total gain at zenith angles 0 and 90 degrees is greater for the 75 mm and 100 mm than the 50 mm model, but all are still less than 0.1 dB. The total gain vs. zenith angle for the different half elliptical bowtie models are displayed in Figure 5.7.

As the width of the half elliptical models decrease, a slight increase in transmit-to-receive isolation is obtained (see Figure 5.10). The most isolation is achieved by the 50 mm width model, which ranges from 27 dB at 228 MHz to 31 dB at 260 MHz. The 75 mm width model performs the second best with values between 27 dB at 228 MHz and 31 dB at 267 MHz. The 100 mm width model performs the worst with a minimum isolation of 27 dB at 227 MHz and a maximum of 31 dB at 271 MHz.

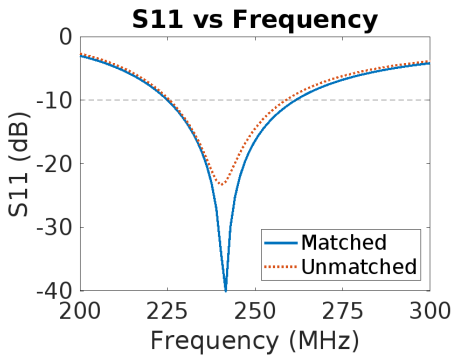

(a) S_{11} vs. frequency
width = 50 mm
length = 248 mm

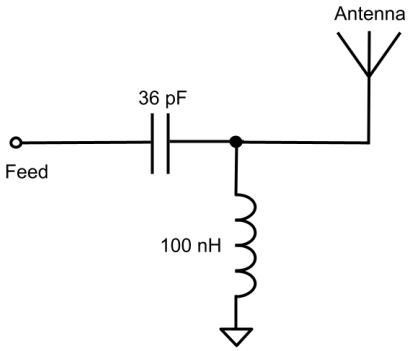

(b) Matching network
width = 50 mm
length = 248 mm

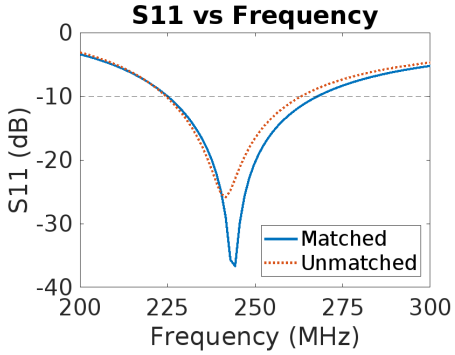

(c) S_{11} vs. frequency
width = 75 mm
length = 240 mm

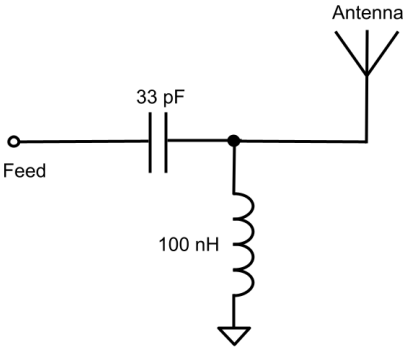

(d) Matching network
width = 75 mm
length = 240 mm

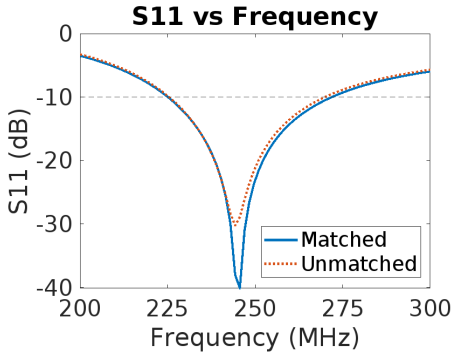

(e) S_{11} vs. frequency
width = 100 mm
length = 231 mm

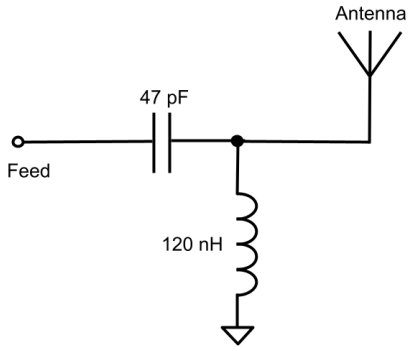

(f) Matching network
width = 100 mm
length = 231 mm

Figure 5.8: The S_{11} vs. frequency plots for the simulated matched and unmatched half elliptical bowtie models of different sizes. The matching network circuit diagrams are included to the right of their corresponding plots.

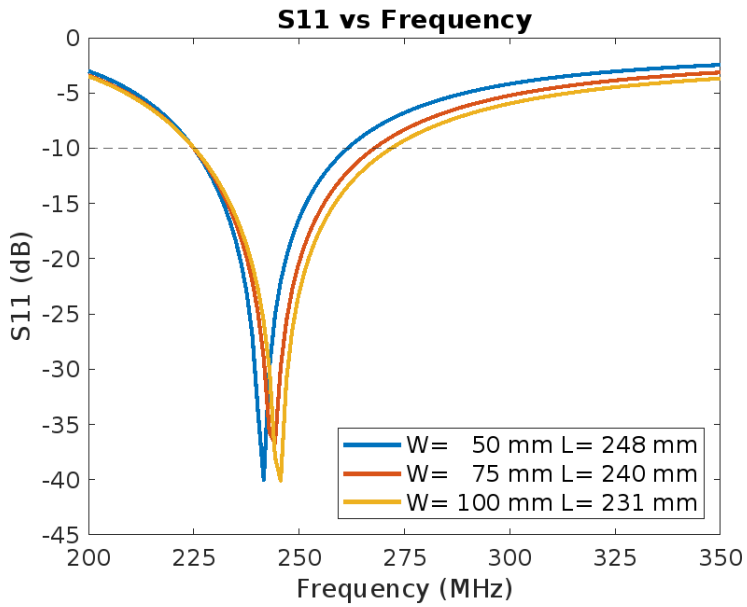

Figure 5.9: The S_{11} vs. frequency plots for the half elliptical bowtie model simulations, where W is the width and L is the length of the half ellipses.

Over the GPR operational range (225 MHz to 255 MHz), the minimum isolation values of the half elliptical bowtie models remain the same, but the maximums are reduced to 30 dB, 29 dB, and 28 dB, for the 50 mm, 75 mm, and 100 mm width models, respectively. The maximum isolation for all three half elliptical bowtie models occur at 255 MHz. The S_{21} versus frequency plots are displayed in Figure 5.10.

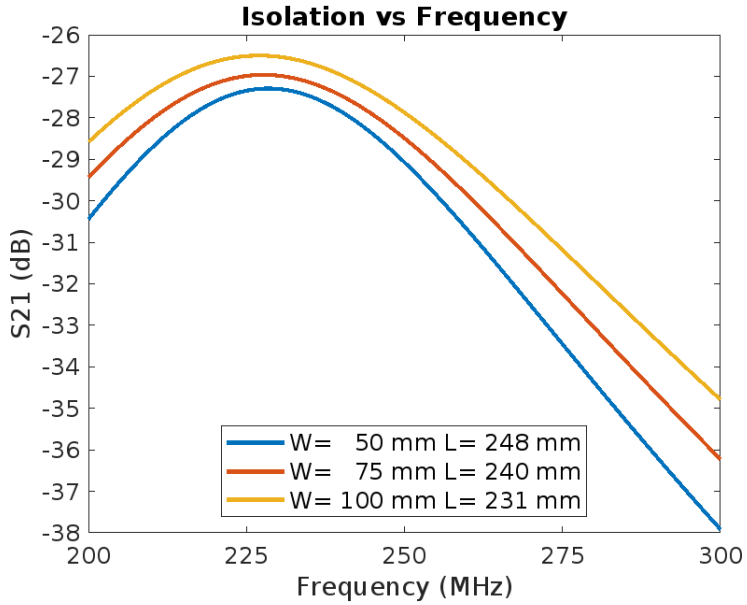

Figure 5.10: The S_{21} vs. frequency plots for the half elliptical bowtie model simulations, where W is the width and L is the length of the half ellipses.

5.3 Elliptical Bowtie Antenna

The copper trace of the elliptical bowtie antenna consists of a full ellipse. The lengths of the ellipses are 270 mm, 265 mm, and 260 mm, which correspond to widths of 50 mm, 75 mm, and 100 mm, respectively. The ellipse sheets are spaced 6 mm apart and small stubs (1.75 mm in width), are added on the inside as a connection point for the source. With the inclusion of the 1 mm edge boundaries and 6 mm spacing, the elliptical bowtie model dimensions are 548 mm x 52 mm x 1 mm, 538 mm x 77 mm x 1 mm, and 528 mm x 102 mm x 1 mm, which correspond to calculated weights (not including mounting structure) of 0.18 lbs, 0.23 lbs, and 0.28 lbs, respectively. The basic structure of the elliptical bowtie model is displayed in Figure 5.11.

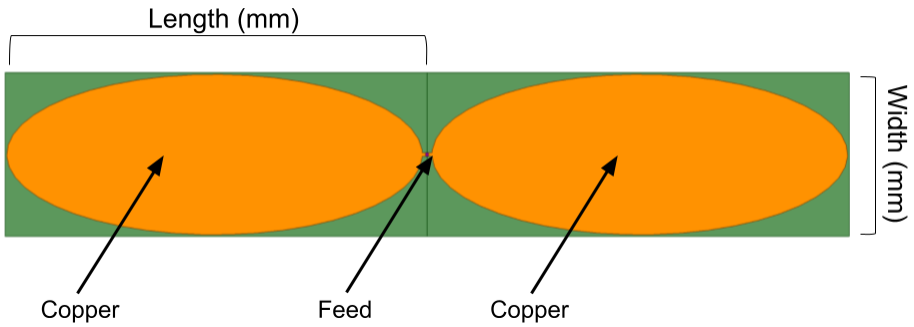

Figure 5.11: The structure of the elliptical bowtie model.

For widths of 50 mm, 75 mm, and 100 mm, the unmatched −10 dB bandwidth is approximately 35 MHz (228 MHz to 263 MHz), 42 MHz (226 MHz to 268 MHz), and 49 MHz (226 MHz to 275 MHz), respectively. With the addition of simple matching networks the bandwidths of the 50 mm, 75 mm, and 100 mm width models increase to approximately 43 MHz (225 MHz to 268 MHz), 50 MHz (225 MHz to 275 MHz), and 53 MHz (225 MHz to 278 MHz), respectively. The S_{11} vs. frequency plots and the matching networks for each configuration are displayed in Figure 5.12. The matched S_{11} plots for the three simulated elliptical bowtie models are included in Figure 5.13.

Over their respective bands of operation, the 50 mm width elliptical bowtie achieves slightly higher isolation than the other two elliptical bowtie models (see Figure 5.14); however, the difference between the performance of all three models is practically negligible. The most isolation is achieved by the 50 mm width model, which has a minimum of 28 dB at 227 MHz and a maximum of 33 dB at 268 MHz. The 75 mm width model performed the second best with a minimum of 28 dB at 225 MHz and a maximum of 30 dB at 275 MHz. The 100 mm width model performed the worst with a minimum isolation of 28 dB at 225 MHz and a maximum of 32 dB at 278 MHz.

Over the band at which the GPR will operate, the minimum isolation values of the elliptical bowtie models remain the same, but the maximums are reduced to approximately 30 dB for all three models. The maximum isolation for the three elliptical bowtie models occur at 255 MHz.

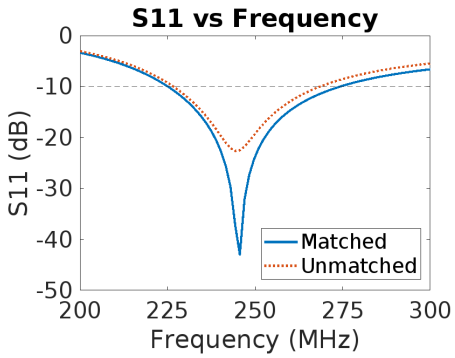

(a) S_{11} vs. frequency
width = 50 mm
length = 270 mm

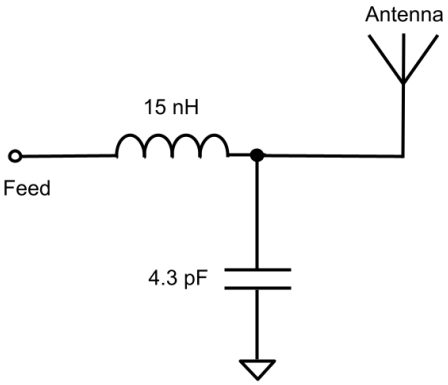

(b) Matching network
width = 50 mm
length = 270 mm

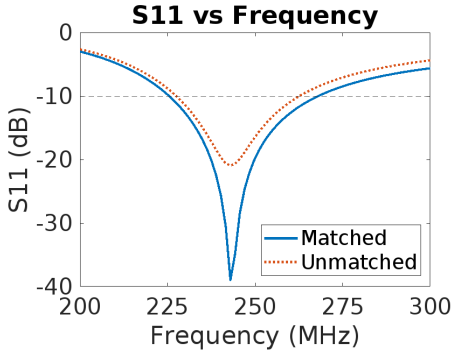

(c) S_{11} vs. frequency
width = 75 mm
length = 265 mm

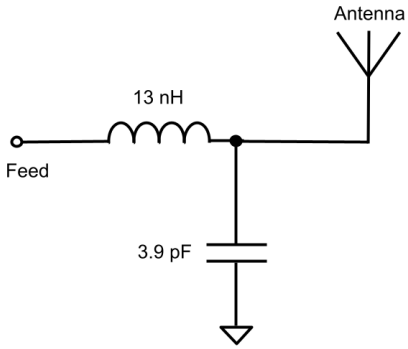

(d) Matching network
width = 75 mm
length = 265 mm

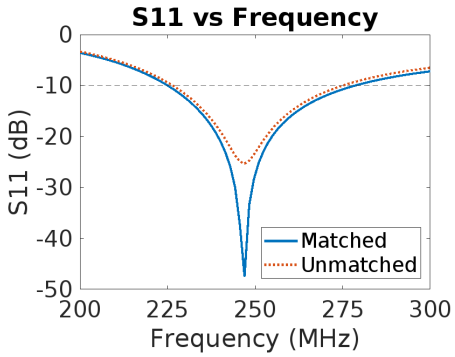

(e) S_{11} vs. frequency
width = 100 mm
length = 260 mm

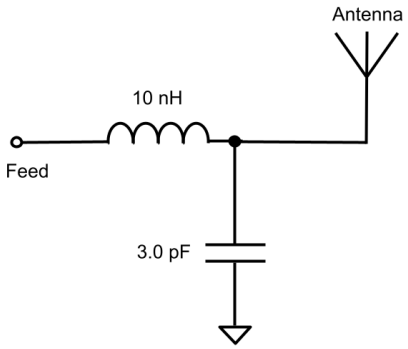

(f) Matching network
width = 100 mm
length = 260 mm

Figure 5.12: The S_{11} vs. frequency plots for the simulated matched and unmatched elliptical bowtie models of different sizes. The matching network circuit diagrams are included to the right of their corresponding plots.

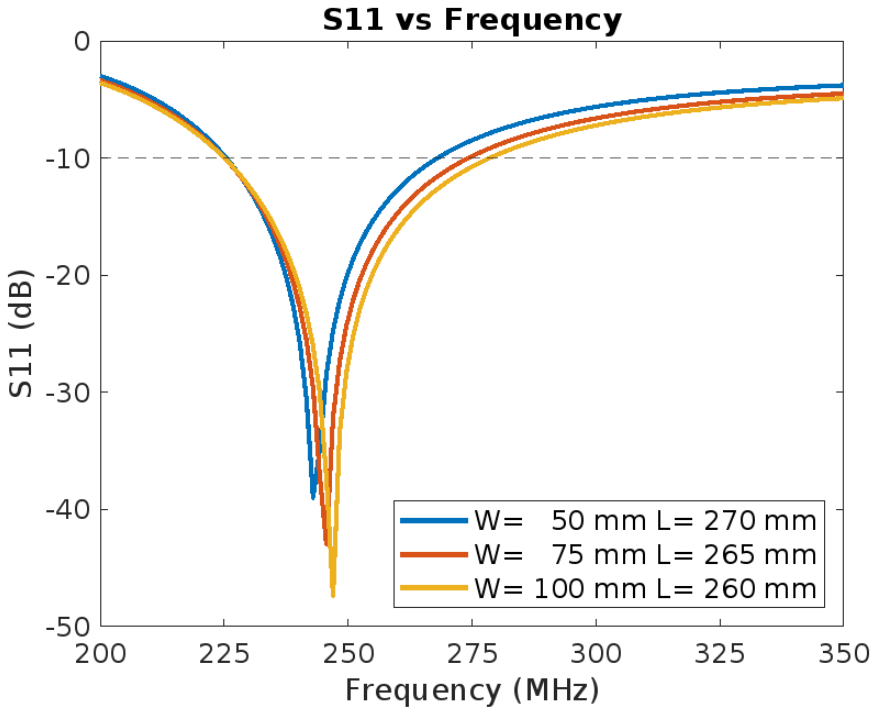

Figure 5.13: The S_{11} vs. frequency plots for the elliptical bowtie model simulations, where W is the width and L is the length of the ellipses.

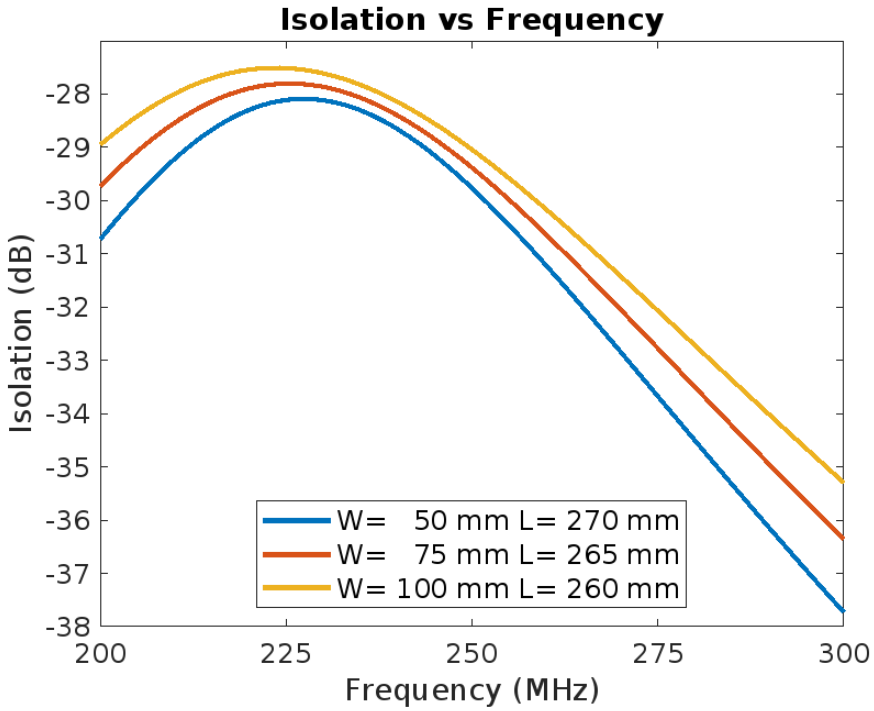

Figure 5.14: The S_{21} vs. frequency plots for the elliptical bowtie model simulations, where W is the width and L is the length of the ellipses.

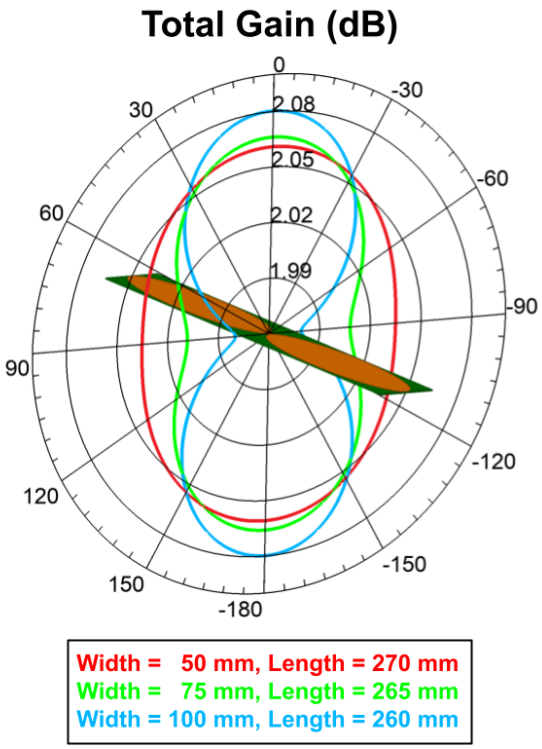

Figure 5.15: The total gain (dB) vs. zenith angle (degrees) at 250 MHz for the 50 mm, 75 mm, and 100 mm width elliptical bowtie model simulations. The total gain is plotted as a field overlay to give context of the orientation of the model.

The total gain of the elliptical bowties at broadside is slightly higher than in the end-fire direction, but the difference for all three models is less than 0.1 dB. At broadside, the 100 mm width model achieves the highest total gain, followed by the 75 mm model, and then the 50 mm model (see Figure 5.15).

5.4 Acorn-Shaped Bowtie Antenna

The acorn-shaped bowtie antenna is a variation of the half elliptical bowtie, where a rounded edge is added to the flat portion of the half ellipse and an additional extension is added on the bottom layer of the substrate (see Figure 5.16). The design in [27], exhibits a relatively compact ultra wide band acorn-shape bowtie antenna model. They used an aluminum backing, in addition to a loop impedance matching network to improve directivity and establish a wider impedance bandwidth. Because we are operating under a weight constraint the aluminum backing is removed and only portions of the acorn-shaped bowtie are used in this design. The model is scaled until it becomes operational at 225 MHz. The dimensions of the antenna are 450 mm x 270 mm x 1 mm. The calculated weight is approximately 0.55 lbs. The scaled model of the simplified version of the acorn-shaped bowtie antenna design can be seen in Figure 5.16.

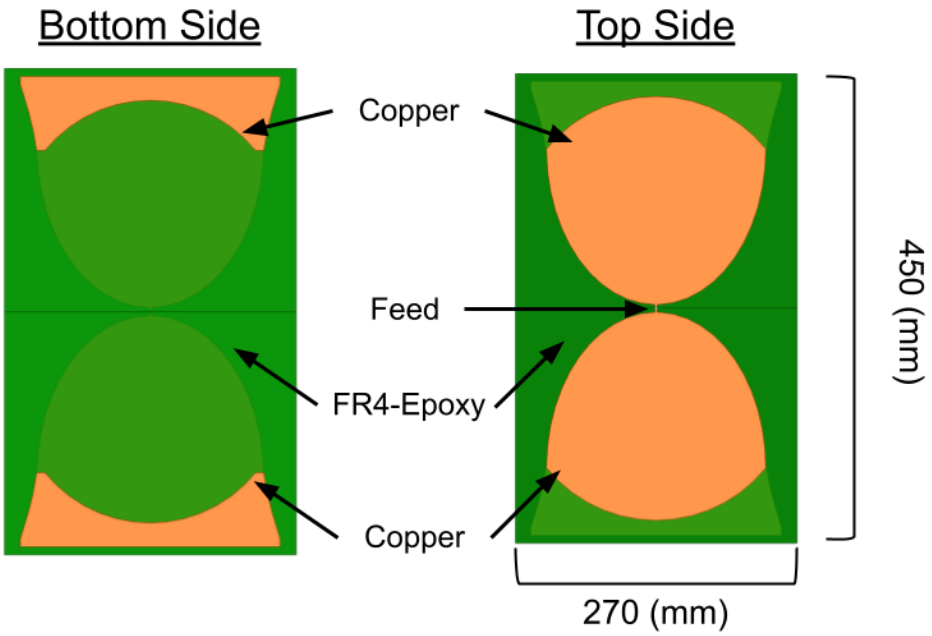

Figure 5.16: The structure of the acorn-shaped bowtie antenna with a bottom side view on the left and a top side view on the right.

The unmatched −10 dB bandwidth is approximately 68 MHz (224 MHz to 292 MHz) without the matching network and 59 MHz (225 MHz to 284 MHz) with the network. The S_{11} vs. frequency plot is displayed in Figure 5.17.

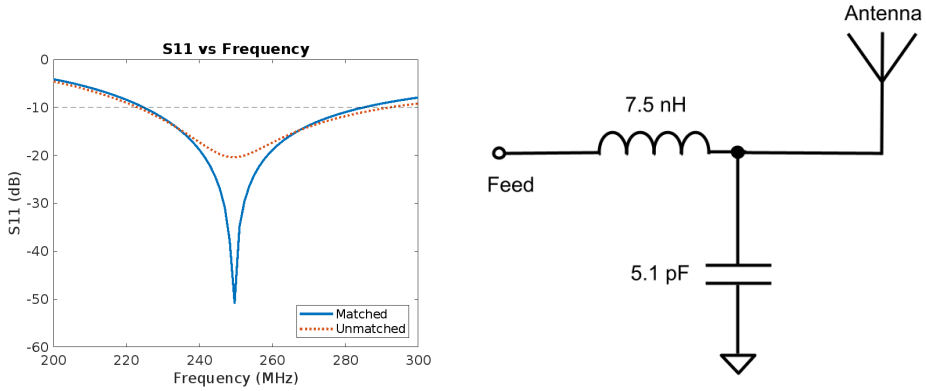

(a) S_{11} vs. frequency (b) Matching network

Figure 5.17: The S_{11} vs. frequency plots for the simulated matched and unmatched acorn-shaped bowtie model. The matching network circuit diagram is included on the right.

Between 225 MHz and 255 MHz, the minimum isolation for the acorn-shaped model is 25 dB and the maximum is 27 dB. Additionally, the peak gain is approximately 2.16 dB at 255 MHz. The S_{21} vs. frequency plot is shown in 5.18. The peak gain vs. frequency plot is displayed in Figure 5.19.

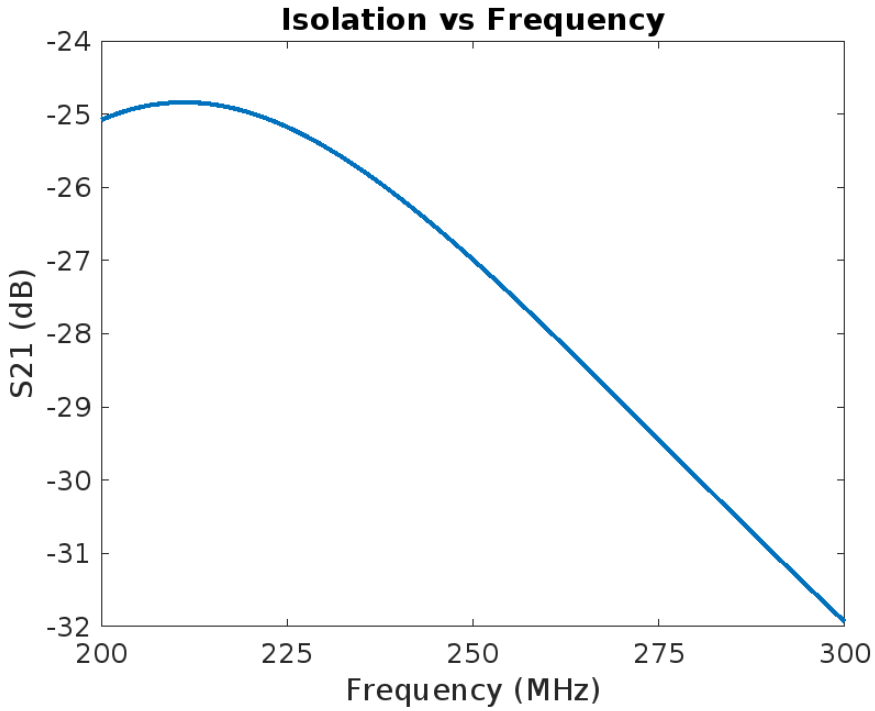

Figure 5.18: The S_{21} vs. frequency plot for the acorn-shaped bowtie model simulation.

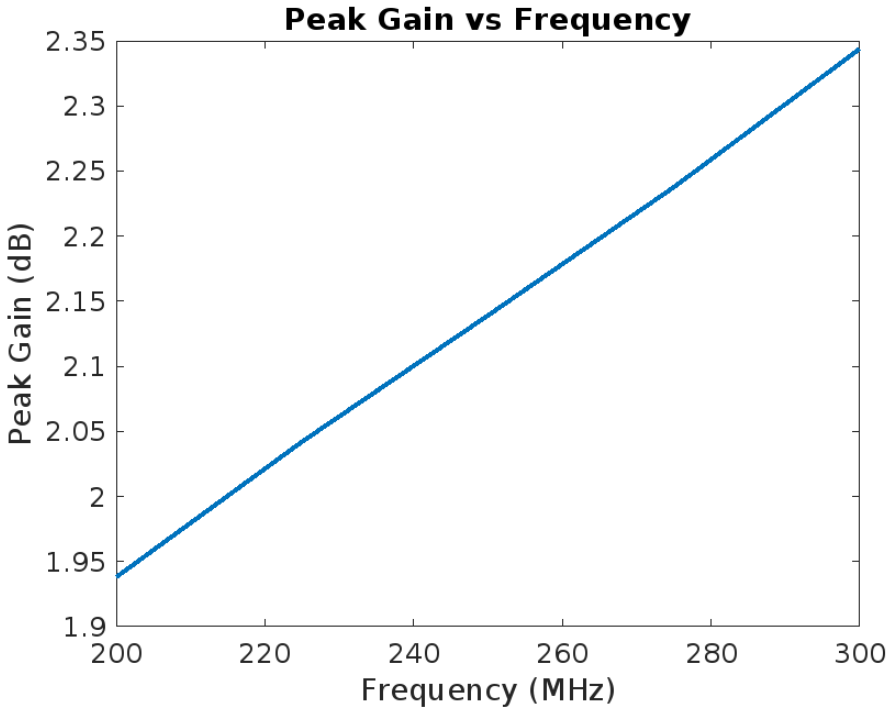

Figure 5.19: The peak gain vs. frequency plot for the acorn-shaped bowtie model simulation.

The geometry of the acorn-shaped model is more complex than the other bowtie models in this chapter so a prototype is made to validate the simulation model. The acorn shaped bowtie is printed in halves and black acrylic blocks are used to connect the two halves to form the antenna. Additionally a green solder mask is applied to the copper traces. With the acrylic connectors and a SMA port, the total weight of the antenna is 0.61 lbs. The constructed models are displayed in Figure 5.20.

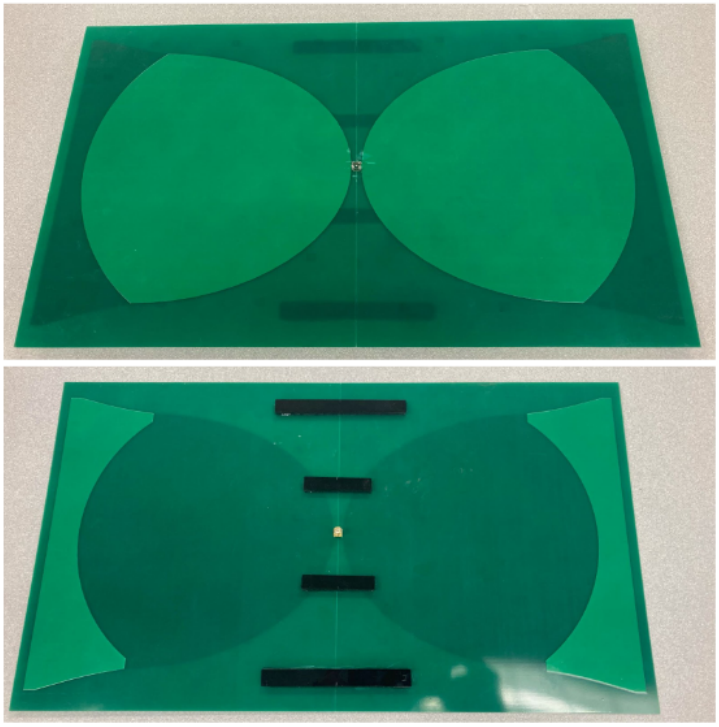

Figure 5.20: The constructed bowtie antenna, where the surfaces are etched copper covered by a solder mask. The black rectangles are pieces of acrylic used to connect the two halves of the antenna.

The S_{11} is measured through the process described in Appendix A. The measured values for the constructed prototypes match the simulation data fairly well. Antenna 1 has an operational bandwidth from 222.75 MHz to 299.25 MHz. Antenna 2 has an operational bandwidth from 216.25 MHz to 300 MHz. The overlap yields a bandwidth of 76.5 MHz from 222.75 MHz to 299.25 MHz. The center frequencies of the constructed models match that of the simulation. The most prominent difference between the measured and simulated models is the reflection coefficient near the center frequency. The S_{11} results for both antennas and the HFSS simulation are contained in Figure 5.21.

The two fabricated antennas were printed professionally to match the size, shape, and material of the simulated model. They are basically identical in structure except that joint where the SMA connector is soldered to the input terminal of Antenna 2 was partially damaged during testing. The

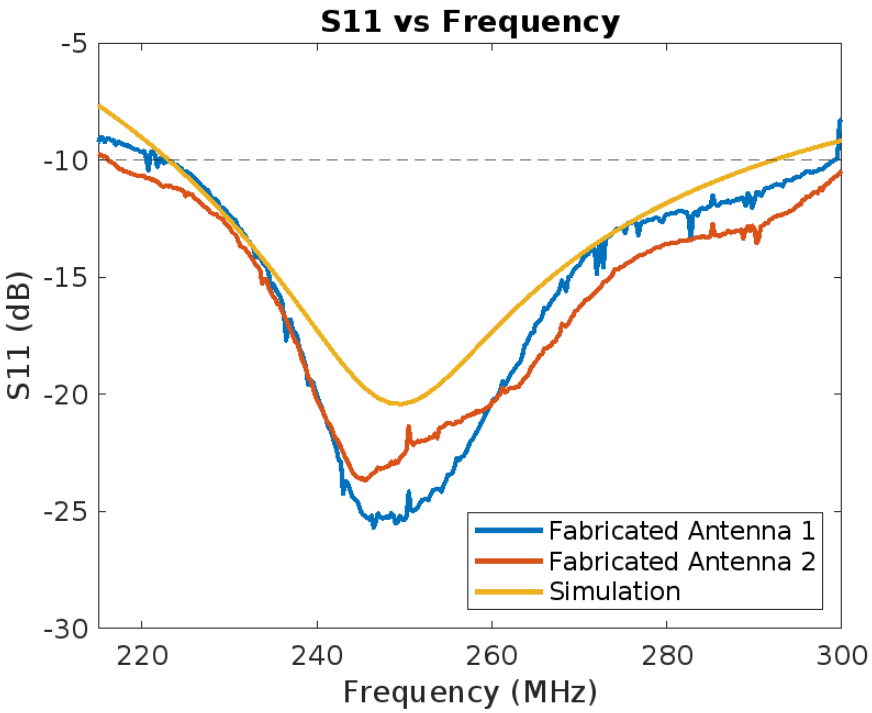

Figure 5.21: The S_{11} vs. frequency plots for the unmatched, constructed acorn-shaped bowtie models. The S_{11} simulation data is included for comparison.

differences in the S_{11} responses of fabricated antennas is most likely due to the damaged terminal. The differences between the simulated model and the fabricated antennas are most likely attributed to the method of measurement and the environment in which the measurement was taken. Overall, the shape of the fabricated S_{11} curves match the simulated model enough to conclude the accuracy of the simulation data.

5.5 Comparison

Out of the ten bowtie models considered in this chapter, only the 50 mm and 75 mm triangular bowties did not meet the 30 MHz bandwidth specifications. The acorn-shaped model exhibits the highest absolute bandwidth, but performs the worst with regard to size and the S_{21}. The elliptical bowtie models out perform the half elliptical and triangular bowties in bandwidth, S_{21}, and gain. The elliptical bowties are slightly longer than the triangular and half elliptical models, but this does not add a significant amount to their calculated weights.

Comparison plots for the S_{11} and S_{21} are displayed in Figure 5.22, where they are grouped by the width of the model. The acorn-shaped model is added to the 100 width model comparison plots. The total gain vs. zenith angle plots are displayed in Figures 5.23 – 5.25. Additionally, Table 5.1 contains the results for the models considered in this chapter, evaluated over the operational band of the GPR.

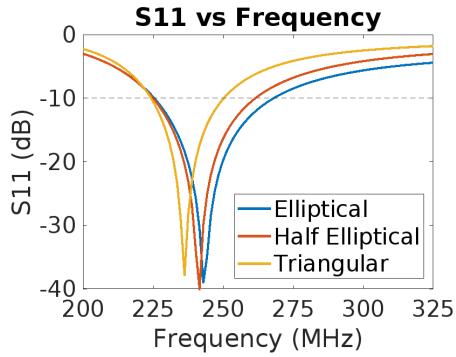

(a) S_{11} vs. frequency
width = 50 mm

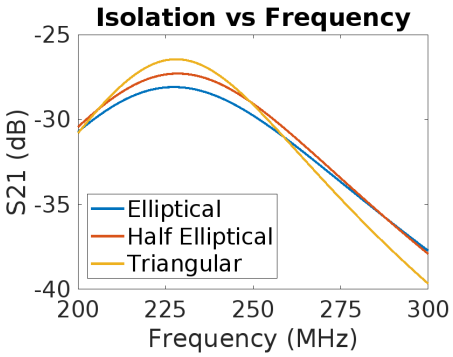

(b) S_{21} vs. frequency
width = 50 mm

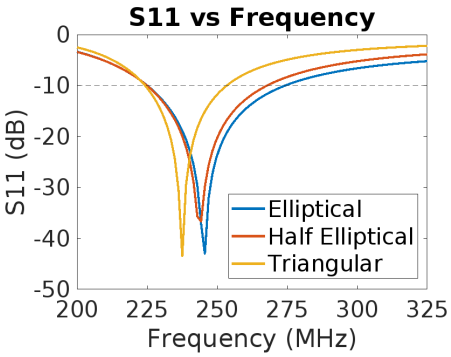

(c) S_{11} vs. frequency
width = 75 mm

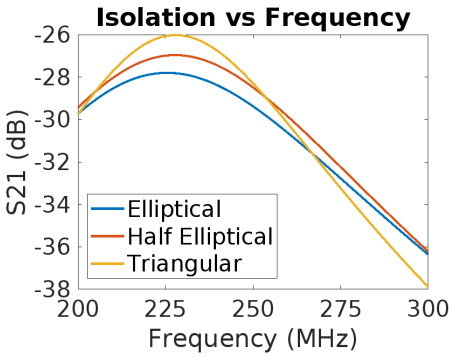

(d) S_{21} vs. frequency
width = 75 mm

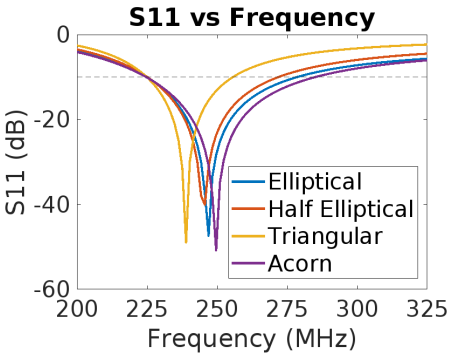

(e) S_{11} vs. frequency
width = 100 mm

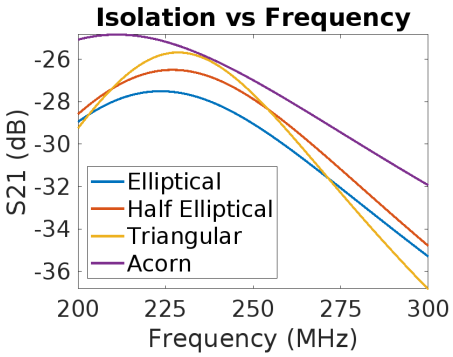

(f) S_{21} vs. frequency
width = 100 mm

Figure 5.22: The S_{11} vs. frequency plots for the triangle, elliptical, half elliptical, and acorn bowtie model simulations of different sizes. The S_{21} plots are included to the right of their corresponding S_{11} plots.

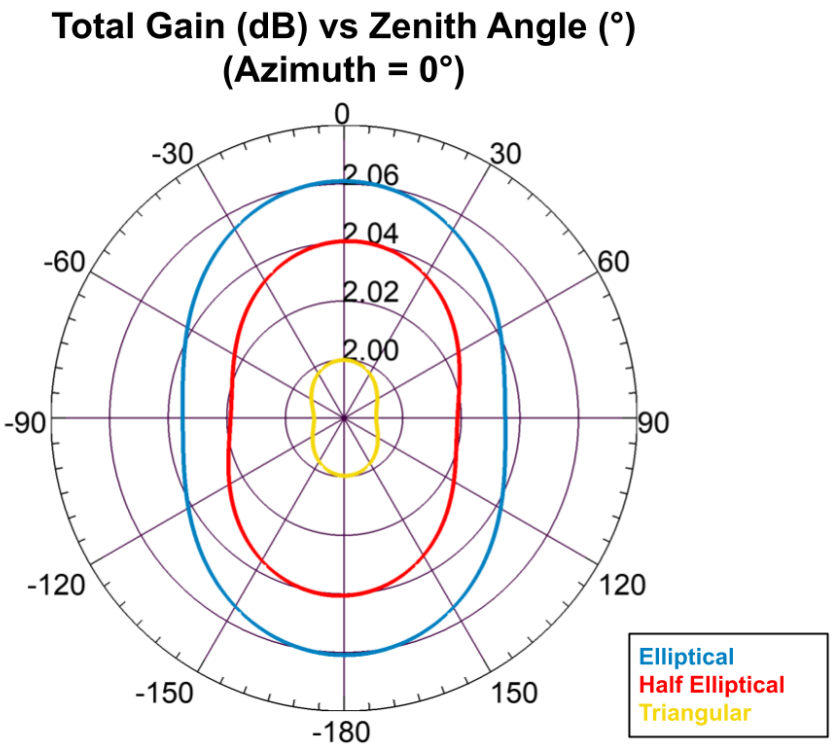

Figure 5.23: The total gain (dB) vs. zenith angle (degrees) at 250 MHz for the 50 mm model simulations.

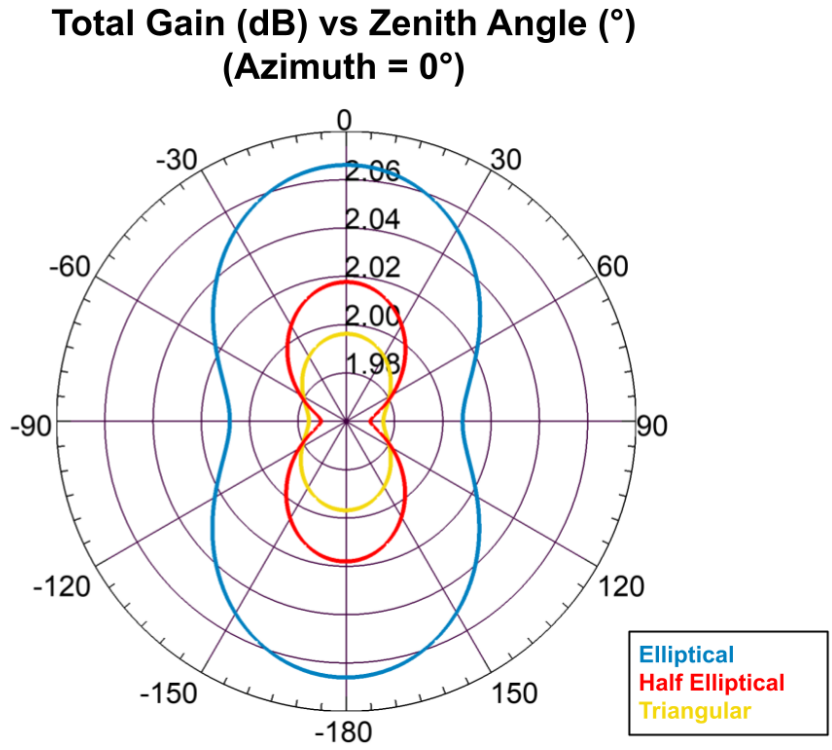

Figure 5.24: The total gain (dB) vs. zenith angle (degrees) at 250 MHz for the 75 mm model simulations.

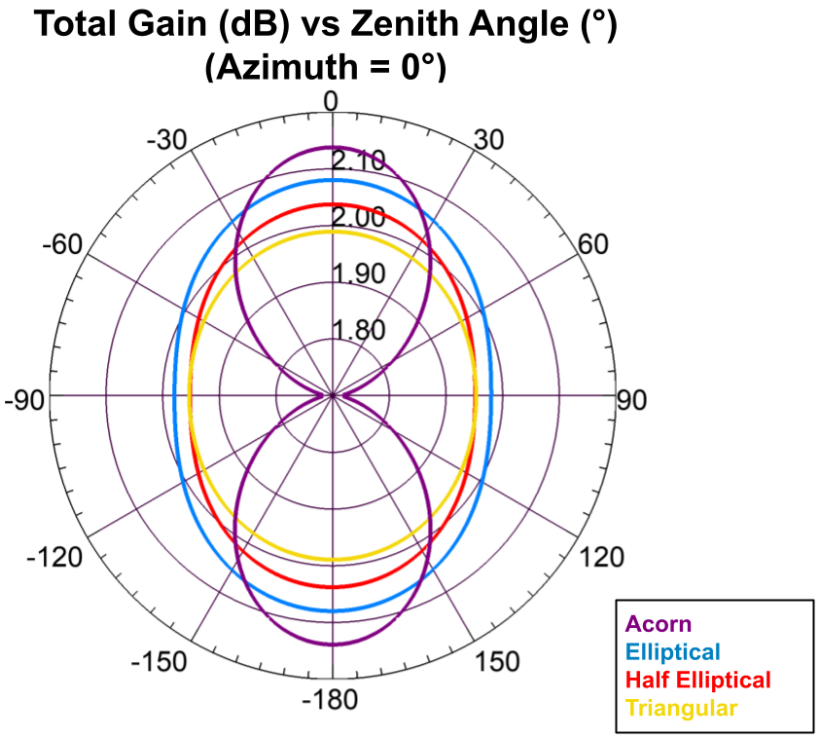

Figure 5.25: The total gain (dB) vs. zenith angle (degrees) at 250 MHz for the 100 mm width model simulations and acorn-shaped model simulation.

Table 5.1: The results for the bowtie antenna simulations. The weight calculations do not include any mounting structure. The minimum isolation, maximum isolation, and maximum gain are calculated over the range in which the GPR will operate (225 MHz to 255 MHz).

Model	Dimensions (mm)	Weight (lbs)	Absolute Bandwidth (MHz)	Fractional Bandwidth (%)	Min Isolation (dB)	Max Isolation (dB)	Max Gain (dB)
Triangular Bowtie	468 x 52 x 1	0.16	24	10.1	26	29	2.01
	448 x 77 x 1	0.20	27	11.3	26	29	2.01
	428 x 102 x 1	0.24	31	12.9	26	29	2.00
Half Elliptical Bowtie	504 x 52 x 1	0.17	35	14.4	27	30	2.06
	488 x 77 x 1	0.21	42	17.1	27	29	2.03
	470 x 102 x 1	0.25	46	19.3	27	28	2.05
Elliptical Bowtie	548 x 52 x 1	0.18	43	17.4	28	30	2.07
	538 x 77 x 1	0.23	50	20.0	28	30	2.08
	528 x 102 x 1	0.28	53	21.1	28	30	2.09
Acorn-Shaped Bowtie	450 x 270 x 1	0.55	59	23.2	25	27	2.16

5.6 Summary

All models in this section meet the 30 MHz bandwidth specifications except for the 50 mm and 75 mm triangular bowtie models. The acorn-shaped bowtie has the widest operational bandwidth, but because it weighs twice as much as the next heaviest model and is significantly larger than all other bowtie models, it is not considered further. The smallest functional model is the 50 mm width half elliptical bowtie. The 50 mm half elliptical bowtie does perform slightly worse than the 50 mm elliptical bowtie with regard to isolation and gain, but the difference is minuscule. Based on the size considerations, the half elliptical bowtie is the best suited for our GPR application; however, if more bandwidth is required, the elliptical bowtie should be considered.

6 Conclusion

6.1 Conclusion

The goal of this research is to create an antenna design that is lightweight, relatively compact, and operational from at least 225 MHz to 255 MHz. In this thesis I considered three classes of simple antennas: dipole, bowtie, and helix. The helix proved to be too large for this application, so I focused on variations of dipole and bowtie designs. All of the considered models meet the bandwidth specification, with the exception of the 50 mm and 75 mm width triangular bowtie antennas. The wire dipole is the most lightweight model and exhibits the most isolation, but barely meets the bandwidth requirement. The next two most light weight models are the 50 mm width half elliptical bowtie and the 50 mm width strip dipole.

The 50 mm strip dipole model is 2.4 cm longer than the half elliptical, but has greater gain, isolation, and bandwidth performance. Currently, the maximum weight allotted for the antennas has not been distinguished from the total weight allotted for the entire radar system. After the weight of the radar and mounting system is determined, a maximum weight specification may be determined for the antennas. If the antenna weight allotment is enough to use the 50 mm strip dipole model, it should be considered because of its bandwidth performance.

The use of the strip dipole could potentially cause issues related to the flight capabilities of the small aircraft. Since the antennas will ultimately be mounted to the bottom of the drone, the size of the antennas need to be small enough that they do not hinder the drones ability to achieve lift. Since the difference between the gain in the broadside and end-fire directions for strip dipole antenna is negligible, the strip dipole antennas could be oriented so that broadside is orthogonal to the plane in which the propellers spin. This would reduce the effect of the antenna on the propeller. Additionally, the width of the strip dipole antenna could be reduced to produce a smaller profile at the cost of bandwidth.

Out of the fifteen models considered in this study, twelve could reasonably be used with our radar system. Out of those twelve models, the 50 mm strip dipole performs the best with regard to bandwidth, while maintaining a weight of only 0.17 lbs. The geometry of the antenna is simple and can easily be altered to achieve variations in the isolation, gain, and bandwidth. Two strip dipole antenna prototypes were built and tested. The measured S_{11} of the fabricated antennas matched the predictions of the simulation. The strip dipole model shows promise and should be considered for future testing.

6.2 Future Work

The constructed 50 mm strip dipole have been used in a preliminary radar test to verify functionality. During the preliminary collections, the transmit-to-receive bleed through signal posed to be a significant issue. For the GPR to function optimally, the coupling between the transmit and receive antennas needs to be reduced so that the transmit-to-receive bleed-though signal does not over power the radar backscatter.

Improvements to the isolation could be made by simply moving the antennas further apart; however, this approach is limited by the vehicle to which the antennas and the necessary mounting structure would be attached. This study demonstrates that there is an improvement in the transmit-to-receive as the width of the antenna is reduced, but this effect is so small that it is insignificant. Alternatively, the placement of light-weight isolation barriers between the transmit and receive antennas could be used to reduce the coupling effects. Higher gain antenna designs should also be considered so that the transmit antenna produces less radiation in the direction of the receive antenna.

References

[1] N. E. Kohls, "Software defined radio short range radar," Master's Thesis, Brigham Young University, June 2021. [Online]. Available: https://search.lib.byu.edu/byu/record/sa.etd.10036.

[2] Anonymous, *Ground Penetrating Radar Theory and Applications*, English, H. M. Jol and P. (Firm), Eds. Elsevier Science, Amsterdam; Boston, 2009. [Online]. Available: https://search.lib.byu.edu/byu/record/cram.110.EBC405936.

[3] M. A. Richards, J. A. Scheer, and W. A. Holm, *Principles of Modern Radar : Basic Principles*, English. 2010, vol. Volume I. [Online]. Available: https://search.lib.byu.edu/byu/record/edsbyu.nlebk.1351399.

[4] F. T. Ulaby, *Microwave Radar and Radiometric Remote Sensing*, English, D. G. Long, W. J. Blackwell, C. Elachi, *et al.*, Eds. The University of Michigan Press, Ann Arbor, 2014, ISBN: 9780472119356. [Online]. Available: https://search.lib.byu.edu/byu/record/cat.6904391.

[5] C. A. Balanis, *Antenna Theory*, English, 2nd ed. Wiley, New York, 1997, ISBN: 0471592684. [Online]. Available: https://search.lib.byu.edu/byu/record/cat.2116701.

[6] K. F. Warnick, *Phased Arrays for Radio Astronomy, Remote Sensing, and Satellite communications*, English. Cambridge University Press, Cambridge, 2018, ISBN: 9781108539258. [Online]. Available: https://search.lib.byu.edu/byu/record/cram.135.CR9781108539258.

[7] J. J. Carr, *Practical Antenna Handbook*, English, 5th ed., G. Hippisley, Ed. McGraw-Hill, New York, 2012, ISBN: 9780071639583. [Online]. Available: https://search.lib.byu.edu/byu/record/cat.5253143.

[8] Y. Huang, *Antennas*, English, K. Boyle, Ed. John Wiley and Sons, Chichester, UK, 2008, ISBN: 9780470772928. [Online]. Available: https://search.lib.byu.edu/byu/record/cram.81.ocn297187083.

[9] *The ARRL Handbook for Radio Communications.* English. 2002, ISBN: 1547-1470. [Online]. Available: https://search.lib.byu.edu/byu/record/cat.3167829.

[10] H. J. Visser, *Antenna Theory and Applications*, English. John Wiley & Sons, Chichester, West Sussex, U.K.; Hoboken, 2012, ISBN: 9781119990253. [Online]. Available: https://search.lib.byu.edu/byu/record/sfx.5503275.

[11] R. Nayak, "Design and analysis of bow-tie antennas for gpr applications," Ph.D. dissertation, 2016. [Online]. Available: http://ethesis.nitrkl.ac.in/9128/3/2016_MT_RNayak.pdf.

[12] H. G. Schantz, "A brief history of uwb antennas," 2003, pp. 209–213. [Online]. Available: https://search.lib.byu.edu/byu/record/edsbyu.edseee.edseee.1267834.

[13] M. R. Islam, "Study and implementation of wideband bow-tie antennas," Ph.D. dissertation, 2017. [Online]. Available: https://search.lib.byu.edu/byu/record/edsbyu.ddu.F469B59B89CD856E.

[14] R. G. L. de Mello, A. C. Lepage, and X. Begaud, "The bow-tie antenna: Performance limitations and improvements," *IET Microwaves, Antennas & Propagation*, vol. 16, no. 5, pp. 283–294, 2022. [Online]. Available: https://search.lib.byu.edu/byu/record/edsbyu.edsdoj.edsdoj.128193f54ee1409796332854abd5978e.

[15] W. L. Stutzman, *Antenna Theory and Design*, English, 3rd ed., G. A. Thiele, Ed. Wiley, Hoboken, NJ, 2013, ISBN: 9780470576649. [Online]. Available: https://search.lib.byu.edu/byu/record/cat.5548477.

[16] R. S. Elliott, *Antenna Theory and Design*, English, Revised ed., I. of Electrical and E. Engineers., Eds. John Wiley & Sons ; IEEE Press, Hoboken, N.J. : Piscataway, N.J., 2003, ISBN: 0471449962. [Online]. Available: https://search.lib.byu.edu/byu/record/sfx.3096925.

[17] G. Kumar, *Helical antennas*, https://www.cdeep.iitb.ac.in/slides/A16/EE609/EE609-L17.pdf, 2000.

[18] P. J. Bevelacqua, *Broadband dipole antenna*. [Online]. Available: https://www.antenna-theory.com/antennas/broaddipole.php.

[19] A. R. Djordjevic, M. M. Ilic, A. G. Zajic, D. I. Olcan, and M. M. Nikolic, "Why does reflector enhance the gain of helical antennas?" English, *Proceedings in the 2nd European Conference of Antennas and Propagation*, pp. 1–8, 2007. [Online]. Available: https://cpn-us-w2.wpmucdn.com/sites.gatech.edu/dist/4/463/files/2015/06/Helix_EuCAP_07.pdf.

[20] X. Tang, B. Feng, and Y. Long, "The analysis of a wideband strip-helical antenna with 1.1 turns.," English, *International Journal of Antennas & Propagation*, pp. 1–7, 2016. [Online]. Available: https://search-lib-byu-edu.erl.lib.byu.edu/byu/record/edsbyu.iih.113627840.

[21] *Helical antennas in satellite radio channel*, 2011. [Online]. Available: https://search.lib.byu.edu/byu/record/edsbyu.edsoai.edsoai.ocn835993828.

[22] A. R. Djordfevic, A. G. Zajic, M. M. Ilic, and G. L. Stuber, "Optimization of helical antennas [antenna designer's notebook]," *IEEE Antennas and Propagation Magazine, Antennas and Propagation Magazine, IEEE, IEEE Antennas Propag. Mag.*, vol. 48, no. 6, pp. 107–115, 2006. [Online]. Available: https://search-lib-byu-edu.erl.lib.byu.edu/byu/record/edsbyu.edseee.edseee.4117993.

[23] D. J. Daniels, W. van Verre, F. Podd, and A. J. Peyton, "Antenna design considerations for ground penetrating radar landmine detection," *IEEE Transactions on Antennas and Propagation, Antennas and Propagation, IEEE Transactions on, IEEE Trans. Antennas Propagat.*, vol. 70, no. 6, pp. 4273–4286, 2022. [Online]. Available: https://search.lib.byu.edu/byu/record/edsbyu.edseee.edseee.9686597.

[24] P. K. Chaudhary, R. Sharma, S. K. Gautam, S. Kumar, and K. P. Ray, "Wide band antenna for ground penetrating radar (gpr)," 2022, pp. 1–4, ISBN: 2766-2101. [Online]. Available: https://search.lib.byu.edu/byu/record/edsbyu.edseee.edseee.9865715.

[25] G. Jinjin, Z. Fuguo, and W. Kan, "A novel ultra wideband resistance loaded bow-tie antenna for ground penetrating radar applications," 2020, pp. 1–3. [Online]. Available: https://search.lib.byu.edu/byu/record/edsbyu.edseee.edseee.9387017.

[26] U. K. Deshmukh, Y. K. Choukikar, and S. B. Naik, "Design of cpw fed bow-tie slot antenna for ground penetrating radar application," 2016, pp. 1820–1823. [Online]. Available: https://search.lib.byu.edu/byu/record/edsbyu.edseee.edseee.7808149.

[27] G. Yang, S. Ye, Y. Ji, X. Zhang, and G. Fang, "Radiation enhancement of an ultrawideband unidirectional folded bowtie antenna for gpr applications," *IEEE Access, Access, IEEE*, vol. 8, pp. 182 218–182 228, 2020. [Online]. Available: https://search.lib.byu.edu/byu/record/edsbyu.edseee.edseee.9214459.

Appendices

A S_{11} Measurement Procedure

The S_{11} is a measurement of how much power is reflected off the input terminal of an antenna due to a mismatch between the impedance of the source and the input impedance of the antenna. Generally it is best to measure the S_{11} with network analyzer; however, our network analyzer is located in an area not suitable for VHF band measurements and we do not have a portable model that can be moved to a different location. Instead, a different approach is taken to measure the S_{11}.

The S_{11} is measured though the use of a spectrum analyzer, signal generator, and a directional coupler. The signal generator connects to the the directional coupler through the port that is furthest away from the others. The spectrum analyzer connects to the coupled port, which is perpendicular to the other two ports. The coaxial cable that is used to connect the antenna to directional coupler is connected to the remaining port.

Before the antenna is connected to the coaxial cable, the spectrum analyzer and the function generator need to be initialized to the desired frequency window and power specifications. Once they are both initialized, a frequency sweep is done with the signal generator and the coupled output is captured. Since the antenna coax is essentially an open circuit, virtually all of the power transmitted by the signal generator reflects off the end of the coax back into the directional coupler. Of the reflected power, -20 dB is coupled into the port that is connected to the spectrum analyzer. This power is used as the baseline reference for the S_{11} measurements.

After the reference collect is completed, the antenna is connected to the coax and another frequency sweep collection initiated. The estimated S_{11} is obtained by subtracting the reference data from the collection data for which the antenna was connected. A diagram demonstrating the equipment setup is shown in Figure A.1.

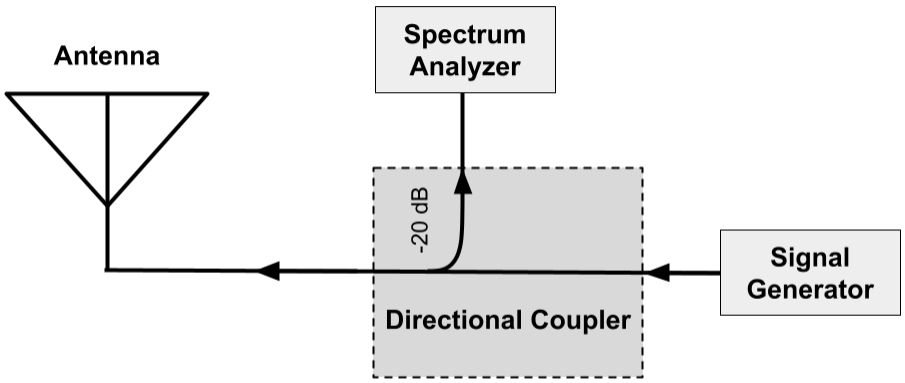

Figure A.1: Diagram of the equipment setup for the S_{11} measurement.